

THESIS FOR THE DEGREE OF LICENTIATE OF PHILOSOPHY

**Microscopic Modeling of Exciton Propagation
and Dissociation in Two-Dimensional
Materials**

Raul Perea-Causin



Department of Physics

CHALMERS UNIVERSITY OF TECHNOLOGY

Göteborg, Sweden 2021

Microscopic Modeling of Exciton Propagation and Dissociation in Two-Dimensional Materials

Raul Perea-Causin

© Raul Perea-Causin, 2021.

Department of Physics
Chalmers University of Technology
SE-412 96 Göteborg
Sweden
Telephone + 46 (0)31-772 1000

Cover illustration: Fundamental processes in a photodetector based on transition metal dichalcogenide (TMD) monolayers with graphene electrodes. (i) Optical excitation and exciton generation, (ii) propagation and transport, (iii) dissociation of excitons into free electrons and holes, (iv) collection of charge-carriers at the electrodes.

Printed at Chalmers Reproservice
Göteborg, Sweden 2021

Microscopic Modeling of Exciton Propagation and Dissociation in Two-Dimensional Materials

Raul Perea-Causin

Department of Physics

Chalmers University of Technology

Abstract

Atomically thin materials have been in the spotlight of research during the last decade due to their exceptional properties, providing a platform for the study of novel physical phenomena. In particular, transition metal dichalcogenides (TMDs) have emerged as promising atomically thin materials for future optoelectronic applications owing to their strong light–matter interaction and their high tunability. Furthermore, the strong Coulomb interaction in TMDs leads to the formation of tightly-bound electron–hole pairs—excitons—that dominate optics, dynamics and transport properties. Therefore, an accurate microscopic description of excitons in TMDs is essential for their technological application.

The aim of this thesis is to microscopically investigate the underlying many-particle mechanisms behind the main processes in optoelectronic devices, such as optical generation and relaxation of excitons as well as their propagation and dissociation into unbound electron-hole pairs. Based on the density matrix formalism, we develop equations of motion describing the dynamics in a system of interacting electrons, phonons, and photons. We investigate the density-dependence of the optical absorption and the thermalization of excitons into so-called dark states. We shed light on exciton propagation, revealing the microscopic mechanisms behind the appearance of spatial rings (halos) in the photoluminescence at strong excitation. Moreover, we tackle the problem of exciton dissociation, providing insights on the prominent role of dark excitons, and examine the tunability and optimal conditions for the efficient operation of TMD-based optoelectronic devices. Finally, we provide microscopic insights on charge separation in WS_2 –graphene heterostructures. Our theoretical work, together with experimental support, contributes to the understanding of the many-particle mechanisms that govern the performance of TMD-based optoelectronic devices.

Keywords: excitons, 2D materials, many-particle physics, propagation, dynamics, dissociation.

List of publications

This thesis consists of an introductory text and the following published articles:

- I. **Exciton propagation and halo formation in two-dimensional materials**
R. Perea-Causín, S. Brem, R. Rosati, R. Jago, M. Kulig, J. D. Ziegler, J. Zipfel, A. Chernikov, E. Malic
Nano Letters 19 (10), 7317 (2019)
- II. **Microscopic modeling of pump–probe spectroscopy and population inversion in transition metal dichalcogenides**
R. Perea-Causín, S. Brem, E. Malic
Physica Status Solidi B 257, 2000223 (2020)
- III. **Phonon-assisted exciton dissociation in transition metal dichalcogenides**
R. Perea-Causín, S. Brem, E. Malic
Nanoscale 13, 1884 (2021)
- IV. **Momentum-resolved observation of exciton formation dynamics in monolayer WS₂**
R. Wallauer, R. Perea-Causin, L. Münster, S. Zajusch, S. Brem, J. Güdde, K. Tanimura, K. Lin, R. Huber, E. Malic, U. Höfer
Nano Letters 21 (13), 5867 (2021)
- V. **Microscopic understanding of ultrafast charge transfer in van der Waals heterostructures**
R. Krause, S. Aeschlimann, M. Chavez-Cervantes, R. Perea-Causín, S. Brem, E. Malic, S. Forti, F. Fabbri, C. Coletti, I. Gierz
In review
arXiv:2012.09268 (2020)

My contribution to the appended publications

As first author in Papers I-III, I developed the theoretical model, performed the numerical evaluations, analyzed the results and wrote the manuscripts with the aid of my main supervisor. In papers IV-V, I developed the theoretical model, performed the numerical evaluations, and analyzed the results as the leading theory author.

Publications not appended in this thesis:

- VI. **Exciton diffusion in monolayer semiconductors with suppressed disorder**
J. Zipfel, M. Kulig, R. Perea-Causín, S. Brem, J. D. Ziegler, R. Rosati, T. Taniguchi, K. Watanabe, M. M. Glazov, E. Malic, A. Chernikov
Physical Review B 101, 115430 (2020)
- VII. **Spatio-temporal dynamics in graphene**
R. Jago, R. Perea-Causín, S. Brem, and E. Malic
Nanoscale 11, 10017 (2019)
- VIII. **Negative effective excitonic diffusion in monolayer transition metal dichalcogenides**
R. Rosati, R. Perea-Causín, S. Brem, E. Malic
Nanoscale 12, 356 (2020)
- IX. **Microscopic picture of electron-phonon interaction in two-dimensional halide perovskites**
D. Feldstein, R. Perea-Causín, S. Wang, M. Dyksik, K. Watanabe, T. Taniguchi, P. Plochocka, E. Malic
The Journal of Physical Chemistry Letters 11 (23), 9975 (2020)
- X. **Temporal evolution of low-temperature phonon sidebands in transition metal dichalcogenides**
R. Rosati, K. Wagner, S. Brem, R. Perea-Causin, E. Wietek, J. Zipfel, J. D. Ziegler, M. Selig, T. Taniguchi, K. Watanabe, A. Knorr, A. Chernikov, E. Malic
ACS Photonics 7 (10), 2756 (2020)
- XI. **Strain-dependent exciton diffusion in transition metal dichalcogenides**
R. Rosati, S. Brem, R. Perea-Causín, R. Schmidt, I. Niehues, S. M. de Vasconcellos, R. Bratschitsch, E. Malic
2D Materials 8, 015030 (2021)
- XII. **The Art of Constructing Black Phosphorus Nanosheet based Heterostructures: from 2D to 3D**
S. Thurakkal, D. Feldstein, R. Perea-Causín, E. Malic, X. Zhang
Advanced Materials 33, 2005254 (2021)

- XIII. **Dark exciton anti-funneling in atomically thin semiconductors**
R. Rosati, R. Schmidt, S. Brem, R. Perea-Causin, I. Niehues, J. Kern,
J. Preuß, R. Schneider, S. M.de Vasconcellos, R. Bratschitsch, E. Malic
In review (2021)
- XIV. **Non-classical exciton diffusion in monolayer WSe₂**
K. Wagner, J. Zipfel, R. Rosati, E. Wietek, J. D. Ziegler, S. Brem, R.
Perea-Causín, T. Taniguchi, K. Watanabe, M. M. Glazov, E. Malic, A.
Chernikov
Physical Review Letters 127, 076801 (2021)
- XV. **Non-equilibrium diffusion of dark excitons in atomically thin
semiconductors**
R. Rosati, K. Wagner, S. Brem, R. Perea-Causín, J. D. Ziegler, J. Zipfel,
T. Taniguchi, K. Watanabe, A. Chernikov, E. Malic
In review
arXiv:2105.10232 (2021)
- XVI. **Dark exciton-exciton annihilation in monolayer transition-metal
dichalcogenides**
D. Erkensten, S. Brem, K. Wagner, R. Gillen, R. Perea-Causín, J. D.
Ziegler, J. Maultzsch, A. Chernikov, E. Malic
In review
arXiv:2106.05035 (2021)

My contribution to the non-appended publications

In paper VI, I developed the theoretical model, performed the numerical evaluations, and analyzed the results as the leading theory author. In the other publications, I took part in developing the theoretical models and analyzing the results during the supervision or in collaboration with the leading theory authors.

Contents

1	Introduction	1
2	Theoretical framework	5
2.1	Density matrix formalism in second quantization	6
2.1.1	Second quantization	6
2.1.2	Hamiltonian in second quantization	6
2.1.3	Equation of motion	11
2.2	Excitons	13
2.2.1	Wannier equation	13
2.2.2	Linear optical response	15
2.2.3	Exciton Hamiltonian	17
3	Optical response	21
3.1	Density-dependent absorption	21
4	Exciton dynamics	25
4.1	Dark-exciton formation	25

5	Exciton propagation	29
5.1	Conventional diffusion	29
5.2	Non-linear propagation and halo formation	31
6	Exciton dissociation	35
6.1	Phonon-assisted dissociation	35
7	Charge transfer	39
7.1	Charge transfer in van der Waals heterostructures	39
8	Conclusion and outlook	43
	Bibliography	47

CHAPTER 1

Introduction

The isolation and characterization of graphene—a single layer of graphite—in 2004 [1] marked the beginning of one of the most exciting journeys in modern physics. This work, which was awarded the Nobel prize in 2010, was the first experimental realization of an atomically-thin material and revealed the extraordinary properties that arise when the motion of electrons is restricted to a two-dimensional plane. Such fascinating discovery opened the way for the study of a large variety of two-dimensional materials that exhibit a plethora of exotic properties [2–8]. Among them, semiconducting transition-metal dichalcogenides (TMDs) stand out as very promising candidates for applications in optoelectronic devices owing to their strong optical absorption/emission and high tunability [6, 9–11]. These materials have the composition MX_2 , and consist of a layer of transition metal atoms ($\text{M}=\text{Mo}, \text{W}$) sandwiched between two layers of chalcogen atoms ($\text{X}=\text{S}, \text{Se}$), overall forming a honeycomb lattice (c.f. Fig. 1.1).

A particular feature of TMDs—and, in general, 2D semiconductors—is the dominant role of excitons [10, 11, 14, 15]. When a photon with sufficiently

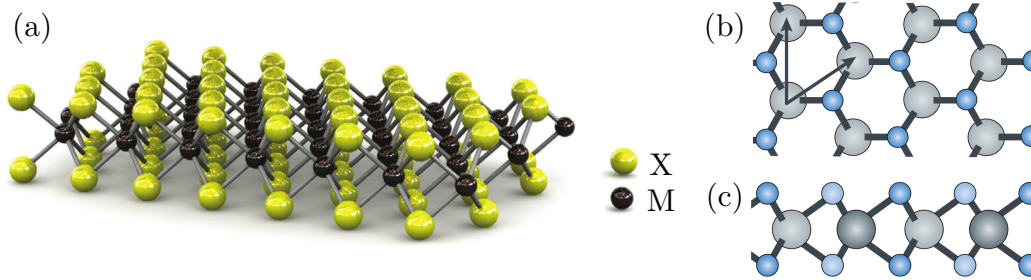


Figure 1.1: (a) Three-dimensional representation of the atomic structure of a TMD monolayer. (b) Top and (c) side perspectives of a TMD monolayer. The arrows represent the lattice vectors. Figures taken from (a) Ref. [12] and (b) Ref. [13].

large energy hits the semiconductor, an electron from the valence band is promoted to the conduction band, leaving behind a positively-charged hole. The attractive Coulomb interaction between the electron and the hole results in a bound electron-hole pair that can be described as a quasi-particle—the exciton—with an energy lower than that of a free electron-hole pair. While in bulk semiconductors excitons play a minor role due to the strongly screened Coulomb interaction, the interaction strength is greatly enhanced by the lower dielectric screening in 2D materials, as illustrated in Fig. 1.2. Additionally, the 2D confinement further increases the binding energy. In consequence, excitons acquire binding energies of hundreds of meV, making them the dominant species governing the material’s properties even at room temperature. The prominent role of excitons is responsible for the exceptional optical properties of TMD monolayers. This distinct signature makes TMDs particularly interesting for optoelectronic applications such as photodetectors, solar cells, and light-emitting devices.

For an effective implementation of TMDs in optoelectronic devices, a microscopic understanding of the fundamental mechanisms governing the main processes in such devices is crucial. In particular, the efficient operation of TMD-based photodetectors or solar cells is ensured by the optimization of the following processes (cf. Fig. 1.3): (i) optical excitation, (ii) propagation or transport, (iii) dissociation of excitons into free electrons and holes and (iv) collection of charge-carriers at the leads and generation of current. A comprehensive study of each of these processes would allow us to determine the best conditions for an optimal operation of these devices and exploit the external tunability of TMDs.

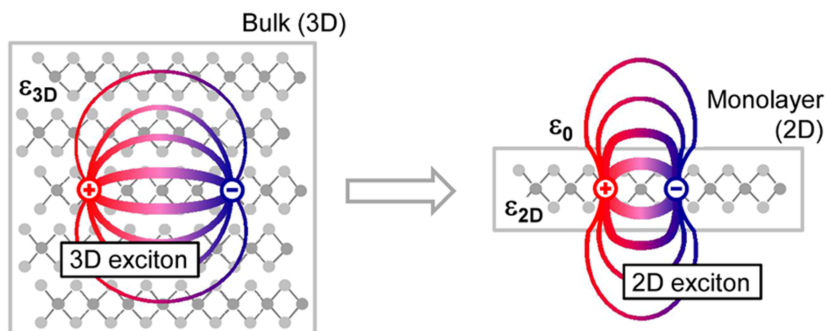


Figure 1.2: Representation of the electron–hole interaction in bulk and monolayers. The electric field lines extending to the vacuum outside of the monolayer are unscreened. In consequence, the dielectric screening in the monolayer is weaker than in bulk. Figure adapted from Ref. [14].

In this thesis, we investigate the underlying mechanisms behind the main processes in TMD-based photodetectors on a microscopic footing. In particular, (1) we study the impact that a finite carrier density has on the optical absorption and reveal the important role of many-particle dielectric screening and Pauli-blocking, which lead to bleaching and spectral shift of the absorption resonances. Moreover, (2) we resolve the exciton dynamics immediately after an optical excitation and provide microscopic insights on the ultra-fast formation of dark excitons. (3) We reveal that the appearance of a ring-like photoluminescence profile after a strong optical excitation arises from the exciton temperature gradient that is caused by Auger scattering and hot phonons. (4) We disentangle the main mechanisms that govern phonon-assisted exciton dissociation and demonstrate the dominant role of dark states. Finally, (5) we show that the asymmetric charge transfer in WS_2 –graphene heterostructures can be traced back to graphene’s pseudospin.

The layout of the thesis is organized as follows. First, we briefly introduce the theoretical framework in Chapter 2. Then, we present our studies regarding each of the specific processes sketched in Fig. 1.3. In Chapter 3, we study how a strong optical excitation alters the absorption spectra of TMDs (Paper II), and in Chapter 4 we discuss the relaxation of excitons into so-called dark states that occurs immediately after an optical excitation (Paper IV). In Chapter 5, we tackle the problem of exciton propagation and, in particular, we unveil the origin of the intriguing ring-shaped photoluminescence profiles

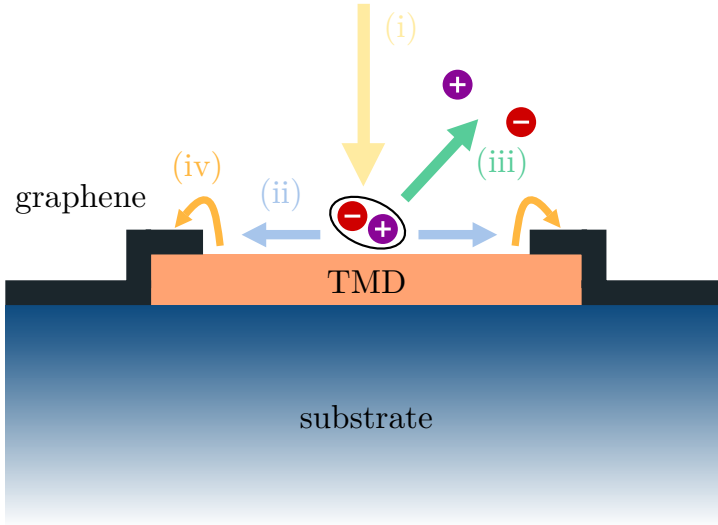


Figure 1.3: Fundamental processes in a TMD-based photodetector with graphene electrodes: (i) Optical excitation and exciton generation, (ii) propagation and transport, (iii) dissociation of excitons into free electrons and holes, (iv) collection of charge-carriers at the electrodes.

that arise at high excitation densities (Paper I). Next, in Chapter 6 we investigate the dissociation of excitons assisted by phonons, which dominates the photoresponse at low electric fields, and identify the important role of dark exciton states (Paper III). In Chapter 7, we study the microscopic origin of the asymmetric charge transfer in WS_2 -graphene interfaces (Paper V), which is closely related to the collection of charge at the leads that occurs in a photodetector. We end with a conclusion and outlook in Chapter 8.

CHAPTER 2

Theoretical framework

In this chapter, we introduce the theoretical framework that allows us to study a many-particle quantum system. First, we present the density matrix formalism in second quantization with a short description of how we obtain equations of motion for microscopic quantities by exploiting the Hamiltonian of the system. After that, we introduce the concept of *exciton* with the exciton basis and Wannier equation, show the influence of exciton states in the optical absorption spectra, and present the exciton Hamiltonian as a useful tool to find the temporal evolution of the exciton population.

2.1 Density matrix formalism in second quantization

2.1.1 Second quantization

An intuitive and convenient treatment of a many-particle quantum system can be obtained by means of the second quantization formalism [16–20], where quantum field operators are expanded in terms of creation (a_i^\dagger) and annihilation (a_i) operators acting on the state i . The fermionic (+) or bosonic (−) character of the particle described by these operators is encoded in the commutation relations

$$\left[a_i, a_j \right]_{\pm} = \left[a_i^\dagger, a_j^\dagger \right]_{\pm} = 0, \quad (2.1)$$

$$\left[a_i^\dagger, a_j \right]_{\pm} = \delta_{ij}, \quad (2.2)$$

where + and − indicate anti-commutation and commutation, respectively. In this framework, any one- or two-particle operator can be expressed as

$$\hat{O}^{(1)} = \sum_{ij} \langle i | \hat{O}^{(1)} | j \rangle a_i^\dagger a_j, \quad (2.3)$$

$$\hat{O}^{(2)} = \frac{1}{2} \sum_{ijlm} \langle i, j | \hat{O}^{(2)} | l, m \rangle a_i^\dagger a_j^\dagger a_l a_m. \quad (2.4)$$

This approach will prove particularly useful for dealing with the Hamiltonian of the system and defining microscopic quantities in a very intuitive way.

2.1.2 Hamiltonian in second quantization

The Hamiltonian is of crucial importance for describing the time evolution of a system. Throughout this work, we consider the scenario of electrons in a solid, i.e. a many-particle problem of interacting electrons, phonons, and photons. Here, we introduce the different parts of the Hamiltonian describing quasi-free electrons in a crystal lattice, phonons, and the electron-electron,

electron–phonon, and electron–light interactions. Note that, since we consider two-dimensional materials, the momentum of electrons and phonons is restricted to the 2D plane.

The Hamiltonian of the system is the sum of several contributions, including free electrons and phonons and the electron–electron, electron–phonon and electron–light interactions,

$$H = H_{e,0} + H_{p,0} + H_{e-e} + H_{e-p} + H_{e-l}. \quad (2.5)$$

Quasi-free electrons in a lattice

The first approach to treating electrons in a crystal is to consider the influence of the potential generated by a static lattice of ions. The motion of electrons in this simple system is characterized by a set of eigen-energies ε_i that form the band structure of the material, where i is a composite index that in general contains the spin and band indices and the momentum vector of the state. The Hamiltonian describing this simple scenario is

$$H_{e,0} = \sum_i \varepsilon_i a_i^\dagger a_i, \quad (2.6)$$

where $a_i^{(\dagger)}$ is the fermionic annihilation (creation) operator for an electron in the state i .

In general, we will be interested in the regions near minima and maxima of the conduction and valence bands, respectively, where the main physics will occur. Minima and maxima of the bands in TMDs occur at the symmetry points of the Brillouin zone denoted by Γ , Λ , K and M (see Fig. 2.1). The band structure around these points can usually be well approximated with a parabolic dispersion, meaning that the electron behaves as a free particle with an effective mass. Throughout this work, we use effective masses and relative energies extracted from bands calculated by density functional theory, in particular from Ref. [21].

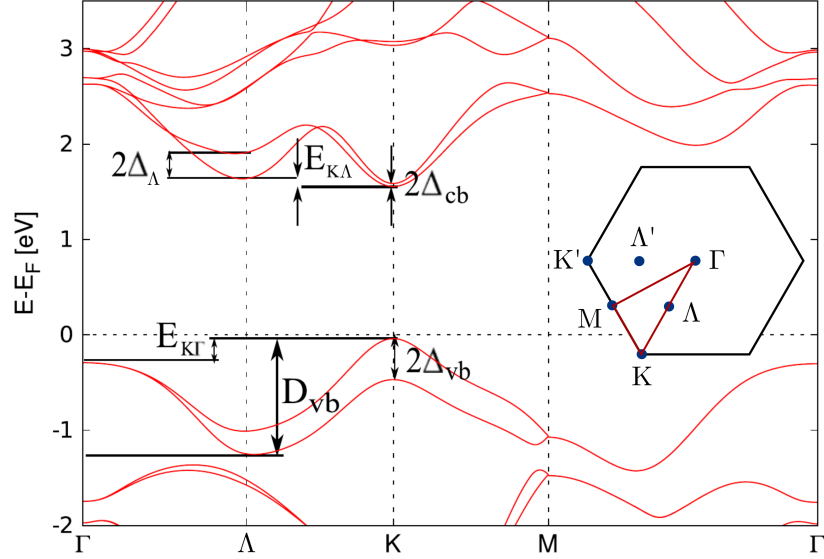


Figure 2.1: Electronic band structure of TMDs. The inset illustrates the symmetry points of the Brillouin zone. The band structure is plotted along the path described by the red line in the inset. Figure adapted from Ref. [21].

Phonons

Phonons are energy quanta of lattice vibrations. Throughout this work, we will see that phonons play an essential role in the relaxation dynamics, assisting electrons/excitons in reaching a thermal distribution. Non-interacting phonons are described by the free-particle Hamiltonian

$$H_{p,0} = \sum_j \hbar\Omega_j b_j^\dagger b_j. \quad (2.7)$$

Here we introduced bosonic annihilation (creation) operators $b_j^{(\dagger)}$ for a phonon in the state j and the phonon energy $\hbar\Omega_j$. The composite index j contains the phonon momentum and mode.

The phonon dispersion relation can be obtained by solving the problem of interacting ions in a lattice. While in general the phonon dispersion can look rather complex, we limit ourselves to momenta around the symmetry points where the minima and maxima of the electronic bands are located. Phonons in these regions will assist the main electronic transitions by scattering with

electrons. Moreover, the dispersion in these regions can be conveniently described with the Debye and Einstein models for acoustic and optical phonons. The energies and sound velocities needed to parametrize the dispersion in these simple models are extracted from *ab initio* calculations in Ref. [22].

Electron-electron interaction

The electron-electron interaction is responsible for major changes in the electron energetic landscape. In particular, the interaction between conduction-band electrons and the absent valence-band electrons (i.e. holes) results in the energetically favourable excitonic states that we discussed in Section 1. The electron-electron interaction is described by the two-particle Hamiltonian

$$H_{e-e} = \frac{1}{2} \sum_{ijklm} V_{lm}^{ij} a_i^\dagger a_j^\dagger a_l a_m. \quad (2.8)$$

Here we introduced the Coulomb matrix element $V_{lm}^{ij} = \langle i, j | V(\mathbf{r}' - \mathbf{r}) | l, m \rangle$, with $V(\mathbf{r}' - \mathbf{r})$ being the Coulomb potential. An analytical treatment of the Coulomb matrix element shows that only momentum- and spin-conserving processes are allowed. Moreover, if we restrict ourselves to intra-band processes with small momentum transfer¹, the Hamiltonian can be written as

$$H_{e-e} = \frac{1}{2} \sum_{\lambda\lambda'\mathbf{k}\mathbf{k}'\mathbf{q}} V_{\mathbf{q}} a_{\lambda,\mathbf{k}+\mathbf{q}}^\dagger a_{\lambda',\mathbf{k}'-\mathbf{q}}^\dagger a_{\lambda',\mathbf{k}'} a_{\lambda,\mathbf{k}}, \quad (2.9)$$

where we introduced the band index $\lambda^{(l)}$ and the momenta $\mathbf{k}^{(l)}$ and \mathbf{q} . The Coulomb matrix element in this case is simply the Fourier transform of the Coulomb potential. For an accurate description of the Coulomb interaction in a TMD monolayer, we consider the finite thickness of the material together with the dielectric properties of the surroundings and solve the corresponding Poisson equation to obtain the potential generated by a charge in the TMD. This potential is sometimes called after Rytova [25] and Keldysh [26] in literature.

¹In general, Coulomb matrix elements depend on material-specific form factors that contain information about the electronic wavefunctions. In the limit considered here, these form factors are close to unity, considerably simplifying the problem. Note that including inter-band processes is necessary for describing Auger scattering and electron-hole exchange (see Paper XVI and Ref. [23, 24]).

electron–phonon interaction

The interaction between electrons and phonons arises in our theory when we consider the interaction of electrons with the lattice beyond the static approximation, i.e. when we take into account the ion vibrations. The corresponding Hamiltonian intuitively illustrates the possible electronic transitions assisted by the emission (b_l^\dagger) or absorption (b_l) of a phonon,

$$H_{\text{e-p}} = \sum_{ijl} \left(g_{ij}^l a_i^\dagger a_j b_l + g_{ij}^{l*} a_j^\dagger a_i b_l^\dagger \right). \quad (2.10)$$

The electron–phonon coupling element reads

$$g_{ij}^l = \sqrt{\frac{\hbar}{2\rho A\Omega_l}} \langle i | \Delta V_l | j \rangle, \quad (2.11)$$

where A is the area of the system, ρ is the mass density of the material, and ΔV_l is the scattering potential. We approximate the scattering potential in zeroth and first order in momentum using the deformation potential approximation. In particular, we extract the deformation potential parameters from ab-initio calculations in Ref. [22].

electron–light interaction

The last important interaction mechanism that we introduce here is that between electrons and light. Since our aim is to describe the optical absorption of the material, it is sufficient to treat light as a classical electromagnetic field. Within this approach, the Hamiltonian describing the electron–light interaction reads

$$H_{\text{e-l}} = -i\hbar \frac{e_0}{m_0} \sum_{ij} \mathbf{M}_{ij} \cdot \mathbf{A}(t) a_i^\dagger a_j, \quad (2.12)$$

where we have introduced the optical matrix element $\mathbf{M}_{ij} = \langle i | \nabla | j \rangle$, the electromagnetic vector potential $\mathbf{A}(t)$, the elementary charge e_0 , the free electron mass m_0 , and the reduced Planck constant \hbar . In general, this Hamiltonian describes intra- or inter-band electronic transitions caused by the absorption of light. Here, we will overall focus on inter-band transitions, i.e. electrons that are promoted from the valence band to the conduction band.

A particular feature of TMDs is circular dichroism [27], which means that K and K' valleys couple to light with opposite circular polarization. This property, combined with the large spin-orbit splitting of the valence bands, implies that electrons in a specific valley and with a specific spin can be selectively excited by choosing the excitation energy and circular polarization. Although this is a very interesting aspect of TMDs, throughout this work we usually consider linearly polarized light, so that electrons in K and K' valleys are equally excited.

2.1.3 Equation of motion

The Hamiltonian of the system gives us direct access to the temporal dynamics of the system. In particular, we can exploit Heisenberg's equation of motion to find the time evolution of an observable O , $i\hbar\frac{dO}{dt} = [O, H]$, where we have assumed that O does not depend explicitly on time. Typically, we are interested in the expectation value $\langle O \rangle$. Using the density matrix $\hat{\rho}$, this expectation value can be easily evaluated as $\langle O \rangle = \text{Tr}(\hat{\rho}O)$. The equation of motion for $\langle O \rangle$ is simply

$$i\hbar\frac{d\langle O \rangle}{dt} = \langle [O, H] \rangle. \quad (2.13)$$

In practice, we will be interested in the temporal evolution of observables such as electron occupation $\rho_{\lambda,\mathbf{k}} = \langle a_{\lambda,\mathbf{k}}^\dagger a_{\lambda,\mathbf{k}} \rangle$, microscopic polarization $p_{\mathbf{k}} = \langle a_{c,\mathbf{k}}^\dagger a_{v,\mathbf{k}} \rangle$, and phonon number $n_{j,\mathbf{q}} = \langle b_{j,\mathbf{q}}^\dagger b_{j,\mathbf{q}} \rangle$. We note already here that when we refer to electrons and holes, we will write the carrier occupations as $f_{\mathbf{k}}^e = \rho_{c,\mathbf{k}}$, $f_{\mathbf{k}}^h = 1 - \rho_{v,\mathbf{k}}$. More details about the equations of motion in the density matrix formalism can be found in Refs. [16, 28].

Cluster expansion

A usual difficulty that appears when treating many-particle systems is the so-called hierarchy problem. If we want to find the temporal evolution of a one-particle quantity, e.g. the electron occupation $\rho_{\lambda,\mathbf{k}}$, we will see that $\rho_{\lambda,\mathbf{k}}$ couples to two-particle expectation values of the form $\langle a_1^\dagger a_2^\dagger a_3 a_4 \rangle$. In order to solve the equation of motion for $\rho_{\lambda,\mathbf{k}}$, we thus need to find the corresponding

equation for $\langle a_1^\dagger a_2^\dagger a_3 a_4 \rangle$, which couples to three-particle quantities, and so on. This would give rise to an infinite number of coupled equations, rendering the problem unsolvable. The solution to this problem is to use the cluster-expansion method [29].

First, we express N -particle quantities in terms of independent single-particle quantities (singlets) and higher-order corrections that account for n -particle correlations, where $n = 2, 3, 4, \dots, N$. After this, we truncate the system to account for a relevant number of correlated particles that allows us to solve the equation of motion. A typical example of the cluster expansion and truncation is the Hartree-Fock approximation, where the two-electron expectation value $\langle a_1^\dagger a_2^\dagger a_3 a_4 \rangle$ is expanded in terms of singlets,

$$\langle a_1^\dagger a_2^\dagger a_3 a_4 \rangle = \langle a_2^\dagger a_3 \rangle \langle a_1^\dagger a_4 \rangle - \langle a_1^\dagger a_3 \rangle \langle a_2^\dagger a_4 \rangle + \langle a_1^\dagger a_2^\dagger a_3 a_4 \rangle^{\text{corr}}, \quad (2.14)$$

and the two-particle correlation $\langle a_1^\dagger a_2^\dagger a_3 a_4 \rangle^{\text{corr}}$ is neglected. This particular example simplifies the system to a single-electron problem, where the interaction with other electrons is approximated as a mean field. For this reason, this specific example is also called *mean-field approximation*.

Markov approximation

A way of including higher-order correlations in a solvable way is to use the Markov approximation. Let us take the problem of electron-phonon scattering as an example. When considering the electron-phonon interaction in the equation of motion for the electron occupation $\rho_{\lambda, \mathbf{k}}$, we will see that $\rho_{\lambda, \mathbf{k}}$ couples to a two-particle correlation of the type $S = \langle a_1^\dagger a_2 b_3 \rangle^{\text{corr}}$, describing an electronic transition from state 2 to 1 assisted by the absorption of a phonon in state 3. The equation of motion for S will have the form

$$\dot{S}(t) = (i\omega - \gamma)S(t) + Q(t). \quad (2.15)$$

The analytical solution to this equation is

$$S(t) = \int_0^\infty d\tau e^{(i\omega - \gamma)\tau} Q(t - \tau). \quad (2.16)$$

The Markov approximation consists in neglecting the past values of Q , i.e. assuming $Q(t - \tau) \approx Q(t)e^{-i\omega_Q\tau}$. Although we neglect the memory of Q , note

that we take into account its temporal oscillation with frequency ω_Q , which is essential for properly capturing the energy conservation of the scattering process. Then, this complicated integral can easily be solved and we obtain

$$S(t) = \frac{Q(t)}{\gamma + i(\omega - \omega_Q)}. \quad (2.17)$$

In the limit where the decay rate γ goes to zero, the Sokhotski–Plemelj theorem can be applied to obtain

$$S(t) = \pi Q(t) \delta(\omega - \omega_Q) - i\mathcal{P} \left(\frac{Q(t)}{\omega - \omega_Q} \right). \quad (2.18)$$

Here \mathcal{P} denotes the Cauchy principal value. When $S(t)$ is plugged back in the equation of motion for the corresponding single-particle quantity (e.g. electron occupation or phonon number), the first term will usually give rise to a scattering rate with exact energy conservation, while the second one will result in an energy renormalization. In general, we will neglect this energy renormalization term, assuming that it is already accounted for in the single-particle energies and that the system is sufficiently close to equilibrium.

2.2 Excitons

In the previous section we have introduced the tools that allow us to study a many-particle quantum system. Here, we will provide the particular example of optical excitation in a semiconductor with the aim of introducing excitons in our theoretical framework.

2.2.1 Wannier equation

An optical excitation in a semiconductor generates a microscopic polarization $p_{\mathbf{k}}$ between the valence and conduction bands. The absolute squared value of this quantity can be regarded as the probability for a valence-band electron to be promoted to the conduction band. The equation of motion for a general $p_{\mathbf{k}_1 \mathbf{k}_2} = \langle a_{\mathbf{c}, \mathbf{k}_1}^\dagger a_{\mathbf{v}, \mathbf{k}_2} \rangle$, including the electron–electron and electron–light

interactions, reads

$$i\hbar\dot{p}_{\mathbf{k}_1\mathbf{k}_2}(t) = (\varepsilon_{\mathbf{k}_2}^v - \varepsilon_{\mathbf{k}_1}^c) p_{\mathbf{k}_1\mathbf{k}_2}(t) + \sum_{\mathbf{q}} V_{\mathbf{q}} p_{\mathbf{k}_1+\mathbf{q},\mathbf{k}_2+\mathbf{q}}(t) + \Omega_{\mathbf{k}_1}(t) \delta_{\mathbf{k}_1\mathbf{k}_2}, \quad (2.19)$$

where we have assumed a full valence band and an empty conduction band. This equation is referred to as semiconductor Bloch equation [28]. The first term describes the oscillation of $p_{\mathbf{k}_1\mathbf{k}_2}$ with a frequency corresponding to the energy of a free electron–hole pair. The second term is a self-coupling of the polarization that results from the Coulomb attraction between conduction-band electrons and valence-band holes. Finally, the last term accounts for the optical generation of polarization via the Rabi frequency $\Omega_{\mathbf{k}}(t) = i\hbar\frac{e_0}{m_0}\mathbf{M}_{\mathbf{k}}^{cv} \cdot \mathbf{A}(t)$, only allowing momentum-conserving transitions due to the small momentum of the incident photons.

In order to simplify this equation, it is convenient to move from electron–hole coordinates $\mathbf{k}_1, \mathbf{k}_2$ to center-of-mass and relative coordinates $\mathbf{Q} = \mathbf{k}_1 - \mathbf{k}_2$, $\mathbf{k} = \alpha_h\mathbf{k}_1 + \alpha_e\mathbf{k}_2$, where $\alpha_l = m_l/(m_h + m_e)$, $l = e, h$. In this coordinate system, equation (2.19) becomes

$$i\hbar\dot{p}_{\mathbf{Q}\mathbf{k}}(t) = -\varepsilon_{\mathbf{Q}\mathbf{k}} p_{\mathbf{Q}\mathbf{k}}(t) + \sum_{\mathbf{q}} V_{\mathbf{q}} p_{\mathbf{Q},\mathbf{k}+\mathbf{q}}(t) + \Omega_{\mathbf{k}}(t) \delta_{\mathbf{Q},0}, \quad (2.20)$$

where $\varepsilon_{\mathbf{Q}\mathbf{k}}$ is the free electron–hole energy in center-of-mass and relative coordinates. Now, we expand the microscopic polarization $p_{\mathbf{Q}\mathbf{k}} = \sum_{\nu} \phi_{\mathbf{Q}\mathbf{k}}^{\nu} P_{\mathbf{Q}}^{\nu}$ in a basis of wavefunctions that are solutions of the electron–hole eigenvalue problem,

$$\varepsilon_{\mathbf{Q}\mathbf{k}} \phi_{\mathbf{Q}\mathbf{k}}^{\nu} - \sum_{\mathbf{q}} V_{\mathbf{q}} \phi_{\mathbf{Q},\mathbf{k}+\mathbf{q}}^{\nu} = \tilde{E}_{\mathbf{Q}}^{\nu} \phi_{\mathbf{Q}\mathbf{k}}^{\nu}, \quad (2.21)$$

with eigen-energy $\tilde{E}_{\mathbf{Q}}^{\nu}$. At the vicinity of the symmetry point corresponding to the valley v , the free electron–hole energy can be written in the effective-mass approximation, $\varepsilon_{\mathbf{Q}\mathbf{k}} = E_g + \frac{\hbar^2(\mathbf{Q}-\mathbf{Q}_v)^2}{2M_v} + \frac{\hbar^2\mathbf{k}^2}{2\mu_v}$, where E_g is the band gap, \mathbf{Q}_v is the valley momentum, $M = m_h + m_e$ is the total exciton mass, and $\mu = \frac{m_e m_h}{M}$ is the exciton reduced mass. In the following we shift $\mathbf{Q} \rightarrow \mathbf{Q} + \mathbf{Q}_v$ to simplify the equations. Since the eigen-value equation above now has a trivial \mathbf{Q} -dependence for each valley, the wavefunctions can be rewritten as $\phi_{\mathbf{Q}\mathbf{k}}^{\nu} \rightarrow \phi_{v\mathbf{k}}^{\nu}$, where the \mathbf{Q} -dependence is now just valley-dependence. These wavefunctions satisfy

$$\frac{\hbar^2\mathbf{k}^2}{2\mu_v} \phi_{v\mathbf{k}}^{\nu} - \sum_{\mathbf{q}} V_{\mathbf{q}} \phi_{v,\mathbf{k}+\mathbf{q}}^{\nu} = E_v^{\nu} \phi_{v\mathbf{k}}^{\nu}. \quad (2.22)$$

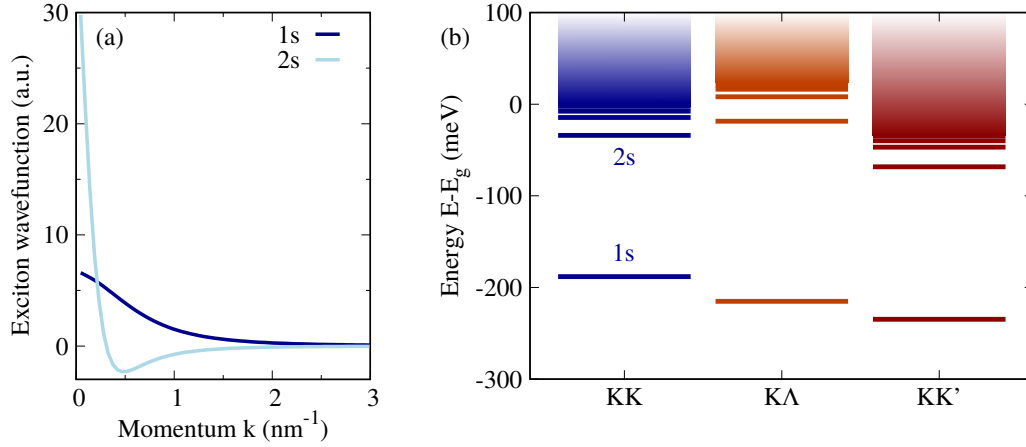


Figure 2.2: Excitons in WS_2 . (a) Exciton wavefunction of 1s and 2s states in the KK valley. (b) Exciton energy landscape including bright (KK) and momentum-dark (K Λ , KK') states.

This is the Schrödinger equation for an electron and a hole in momentum space, and is commonly referred to as Wannier equation. In analogy to the problem of an electron in a hydrogen atom, the attractive interaction between electrons and holes results in a series of bound electron–hole (exciton) states with binding energies E_v' , up to the scattering continuum where electrons and holes are not bound (see Fig. 2.2(b)). The exciton wavefunctions (Fig. 2.2(a)) resemble those of the hydrogen atom, although we remark here that the whole series of exciton states in a TMD cannot be described by the hydrogen model because of the non-local (momentum-dependent) dielectric function that arises from the finite TMD thickness. Due to the different binding energies in separate valleys, the exciton landscape can significantly differ from its free-electron counterpart. In particular, while the free electron–hole energy in the K Λ valley is above that of KK, this situation is reversed in the exciton landscape of tungsten-based TMDs.

2.2.2 Linear optical response

The effect that an external electric field \mathbf{E} has on a material is to induce a polarization \mathbf{P} . The linear response of the material is $\mathbf{P}(\omega) = \epsilon_0 \chi(\omega) \mathbf{E}(\omega)$, where χ is the electric susceptibility tensor, which we have assumed to be

isotropic. Using the relation between the electric field and the vector potential, $\mathbf{E} = -\dot{\mathbf{A}}$, and between the polarization and the current density, $\mathbf{j} = \dot{\mathbf{P}}$, the susceptibility can be written as

$$\chi(\omega) = \frac{P(\omega)}{\epsilon_0 E(\omega)} = \frac{j(\omega)}{\epsilon_0 \omega^2 A(\omega)} \quad (2.23)$$

The imaginary part of the susceptibility describes the optical absorption of the material. The current density in second quantization reads

$$\mathbf{j}(t) = \frac{e_0}{2Am_0} \sum_{ij} \langle i | (-i\hbar\nabla) | j \rangle \langle a_i^\dagger a_j \rangle (t) = \frac{e_0 \hbar}{Am_0} \sum_{\mathbf{k}} \text{Im} \{ \mathbf{M}_{\mathbf{k}} p_{\mathbf{k}\mathbf{k}}(t) \}, \quad (2.24)$$

where we have omitted the intra-band current that becomes important only at THz frequencies. The microscopic polarization thus determines the optical absorption.

In the following, we omit the valley index v for simplicity. Using the orthonormality of the exciton wavefunctions, the equation of motion for the excitonic polarization $P_{\mathbf{Q}}^\nu$ can be shown to be

$$i\hbar \dot{P}_{\mathbf{Q}}^\nu(t) = \left(E_g + \frac{\hbar^2 \mathbf{Q}^2}{2M} + E^\nu - i\gamma \right) p_{\mathbf{Q}}^\nu(t) + \Omega^\nu(t) \delta_{\mathbf{Q},0}, \quad (2.25)$$

where we have introduced the excitonic Rabi frequency, $\Omega^\nu(t) = \sum_{\mathbf{k}} \phi_{\mathbf{k}}^{\nu*} \Omega_{\mathbf{k}}(t)$, and the phenomenological damping γ . The excitonic polarization in frequency space can be directly solved by Fourier-transforming the equation above. Plugging the result in Eqs. (2.24) and (2.23) results in the so-called Elliot formula [29] for the optical absorption α ,

$$\alpha(\omega) \propto \frac{1}{\omega} \sum_{\nu} \frac{|M^\nu|^2}{(\hbar\omega - E_0^\nu)^2 + \gamma^2}. \quad (2.26)$$

Here we have defined the excitonic optical matrix element $M^\nu = \sum_{\mathbf{k}} \phi_{\mathbf{k}}^{\nu*} M_{\mathbf{k}}$ and the exciton resonance energy $E_0^\nu = E_g + E^\nu$. This formula illustrates very clearly that, due to the electron–hole attraction, optical absorption can occur only at particular energies E_0^ν corresponding to excitonic states ν (see Fig. 2.3). Moreover, assuming a constant optical matrix element, $M_{\mathbf{k}}^{\text{cv}} \approx M_0$, the oscillator strength—intensity of the absorption peak—is given by $|M_0|^2 |\phi^\nu(\mathbf{0})|^2$, where $\phi^\nu(\mathbf{r}) = \sum_{\mathbf{k}} e^{i\mathbf{k}\cdot\mathbf{r}} \phi_{\mathbf{k}}^\nu$ is the probability to find an electron

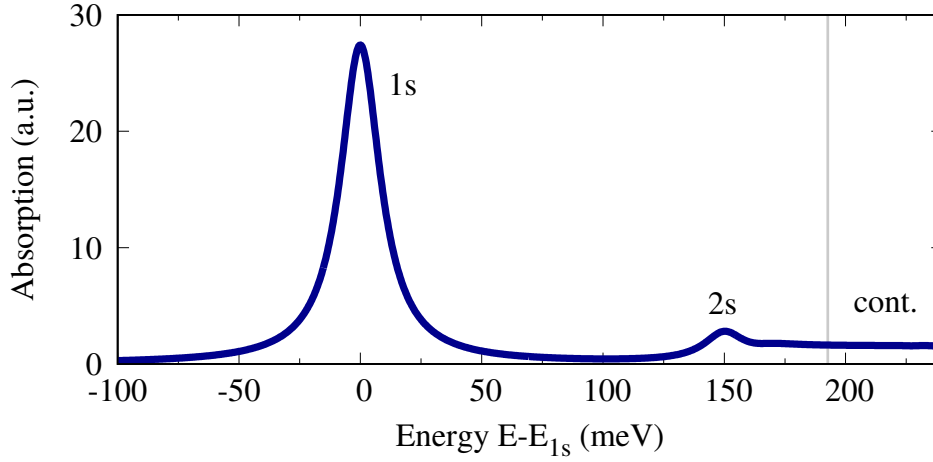


Figure 2.3: Optical absorption calculated for WS_2 encapsulated in hexagonal boron nitride (hBN). The 1s and 2s exciton peaks, as well as the scattering continuum are labeled.

at a distance \mathbf{r} from a hole. The oscillator strength is thus given by the probability of an electron and a hole being at the same position—so that they can recombine. Therefore, the optical absorption at the exciton resonance is stronger for tightly-bound excitons, where the electron and the hole are more likely to be on top of each other.

In Chapter 3, we will discuss how a finite population of electrons and holes can alter the excitonic properties of a two-dimensional semiconductor and, in particular, its optical absorption.

2.2.3 Exciton Hamiltonian

In the previous section we have introduced the exciton basis and the corresponding exciton states. These states can be occupied by electron–hole pairs. The electron–hole expectation value of the type $\langle c^\dagger v v^\dagger c \rangle$ (where $c \equiv a_c$, $v \equiv a_v$) describes the two-particle electron–hole occupation and can be expanded as a sum of singlets $|p|^2 + f^e f^h$ and the correlated doublet $\langle c^\dagger v v^\dagger c \rangle^{\text{corr}}$ (note that we are omitting the momentum index for simplicity). While in the absence of excitonic effects the electron–hole correlation can be neglected, this term dominates the dynamics in an excitonic system such as

TMDs. Therefore, the equations of motion of this quantity must be obtained, which is a lengthy and tedious calculation. A way to make the treatment of the problem easier is to use the exciton expansion scheme introduced in Refs. [30, 31] and find an exciton Hamiltonian, with bosonic annihilation (creation) operators $X_{\mathbf{Q}}^{\nu(\dagger)}$ acting on an exciton at state ν with center-of-mass momentum \mathbf{Q} . The purely bosonic treatment of excitons is sufficient at low densities, while at larger densities the fermionic substructure has to be taken into account, e.g. by including fermionic exchange interactions [30] (see also Paper XVI).

The exciton Hamiltonian including exciton–phonon and exciton–light interactions reads

$$\begin{aligned}
H_x = & \sum_{\nu\mathbf{Q}} E_{\mathbf{Q}}^{\nu} X_{\mathbf{Q}}^{\nu\dagger} X_{\mathbf{Q}}^{\nu} \\
& + \sum_{\nu\mu\mathbf{Q}\mathbf{q}j} \left(G_{j\mathbf{Q}\mathbf{q}}^{\nu\mu} X_{\mathbf{Q}+\mathbf{q}}^{\nu\dagger} X_{\mathbf{Q}}^{\mu} b_{\mathbf{q}}^j + \text{h.c.} \right) \\
& - i\hbar \sum_{\nu} \left(\Omega^{\nu}(t) X_{\mathbf{0}}^{\nu\dagger} + \text{h.c.} \right). \tag{2.27}
\end{aligned}$$

The first term describes the exciton kinetic motion with the energy $E_{\mathbf{Q}}^{\nu} = E_g + E^{\nu} + \frac{\hbar^2 \mathbf{Q}^2}{2M}$. The second term accounts for exciton–phonon interaction, with the matrix element

$$\begin{aligned}
G_{j\mathbf{Q}\mathbf{q}}^{\nu\mu} = & g_{j\mathbf{q}}^{c,v_e^{\nu}v_h^{\mu}} \delta_{v_h^{\nu}v_h^{\mu}} \mathcal{F}^{\mu\nu} (\alpha_{h,\nu}\mathbf{q} + (\alpha_{h,\nu} - \alpha_{h,\mu})\mathbf{Q}) \\
& - g_{j\mathbf{q}}^{v,v_h^{\nu}v_h^{\mu}} \delta_{v_e^{\nu}v_e^{\mu}} \mathcal{F}^{\mu\nu} (-\alpha_{e,\nu}\mathbf{q} - (\alpha_{e,\nu} - \alpha_{e,\mu})\mathbf{Q}). \tag{2.28}
\end{aligned}$$

This matrix element describes the exciton transition $(\mu, \mathbf{Q}) \rightarrow (\nu, \mathbf{Q} + \mathbf{q})$ assisted by a phonon of mode j with momentum \mathbf{q} relative to its valley that is also contained in j . The first term in Eq. (2.28) describes the scattering of an electron, while the second one describes the scattering of a hole, with the index $v_{e(h)}^{\nu}$ referring to the valley where the electron (hole) of the exciton ν lies. Note that when the electron (hole) scatters, the hole (electron) valley is conserved. The electron–phonon matrix elements g are weighted by the excitonic form-factors $\mathcal{F}^{\nu\mu}(\mathbf{q}) = \sum_{\mathbf{k}} \phi_{\mathbf{k}}^{\nu*} \phi_{\mathbf{k}+\mathbf{q}}^{\mu} = \langle \nu | e^{i\mathbf{q}\cdot\mathbf{r}} | \mu \rangle$. In practice, we assume $\alpha_{e(h),\nu} \approx \alpha_{e(h),\mu}$ to get rid of the \mathbf{Q} -dependence of G . Finally, the last term in the Hamiltonian describes the creation or destruction of a bright exciton ($\mathbf{Q} = 0$) by interacting with light.

With this Hamiltonian and the tools described in this chapter (cluster expansion, truncation and Markov approximation), one can now find equations of motion for the exciton occupation $\langle X_{\mathbf{Q}}^{\nu\dagger} X_{\mathbf{Q}}^{\nu} \rangle$. This expectation value can be expanded as the sum of a coherent and an incoherent part, $\langle X_{\mathbf{Q}}^{\nu\dagger} X_{\mathbf{Q}}^{\nu} \rangle = |P_{\mathbf{Q}}^{\nu}|^2 + N_{\mathbf{Q}}^{\nu}$. Here we have introduced the excitonic polarization, $P_{\mathbf{Q}}^{\nu} = \langle X_{\mathbf{Q}}^{\nu\dagger} \rangle$, and the incoherent exciton occupation, $N_{\mathbf{Q}}^{\nu} = \langle X_{\mathbf{Q}}^{\nu\dagger} X_{\mathbf{Q}}^{\nu} \rangle^{\text{corr}}$. The resulting equations of motion are the excitonic analogous of the semiconductor Bloch equations and read

$$\dot{P}^{\nu}(t) = \left(\frac{i}{\hbar} E_0^{\nu} - \frac{1}{2} \sum_{\mu\mathbf{Q}} \Gamma_{0\mathbf{Q}}^{\nu\mu} - \gamma \right) P^{\nu}(t) + i\Omega^{\nu}(t) \quad (2.29)$$

$$\dot{N}_{\mathbf{Q}}^{\nu}(t) = \sum_{\mu} \Gamma_{0\mathbf{Q}}^{\mu\nu} |P^{\mu}(t)|^2 + \sum_{\mu\mathbf{Q}'} (\Gamma_{\mathbf{Q}'\mathbf{Q}}^{\mu\nu} N_{\mathbf{Q}'}^{\mu}(t) - \Gamma_{\mathbf{Q}\mathbf{Q}'}^{\nu\mu} N_{\mathbf{Q}}^{\nu}(t)). \quad (2.30)$$

These equations describe the generation of polarization by the incident light and the subsequent polarization-to-population transfer assisted by phonons. Moreover, exciton-phonon scattering leads to thermalization of the incoherent exciton occupation. The exciton-phonon interaction enters via the scattering matrix

$$\Gamma_{\mathbf{Q}\mathbf{Q}'}^{\nu\mu} = \frac{2\pi}{\hbar} \sum_{j\pm} |G_{j,\mathbf{Q}'-\mathbf{Q}}^{\nu\mu}|^2 \left(n_{\mathbf{Q}'-\mathbf{Q}}^j + \frac{1}{2} \pm \frac{1}{2} \right) \delta(E_{\mathbf{Q}'}^{\mu} - E_{\mathbf{Q}}^{\nu} \pm \hbar\Omega_{\mathbf{Q}'-\mathbf{Q}}^j), \quad (2.31)$$

where $n_{\mathbf{q}}^j$ and $\Omega_{\mathbf{q}}^j$ are the Bose-Einstein distribution and frequency of phonons with phonon mode j and momentum \mathbf{q} and \pm accounts for phonon emission (+) and absorption (-). The scattering matrix provides the strength of each scattering transition and is analogous to Fermi's golden rule. Note that here we have restricted ourselves to one-phonon processes, whereas processes involving more phonons can be considered by including higher-order correlations. This equation is the basis for resolving the exciton dynamics after an optical excitation. Extended versions of this equation will be used in Chapters 4, 5 and 6.

CHAPTER 3

Optical response

The response of a material to an optical excitation is an essential aspect of a photodetector. It is crucial to understand optical absorption and how it is modified by the optical excitation itself in order to determine the optimal conditions and limitations of the material. In this chapter, we introduce Paper II, where we investigate how the optically-generated carrier density modifies optical absorption spectra.

3.1 Density-dependent absorption

In Chapter 2, we showed that the optical absorption is dominated by the excitonic properties of a material, following Elliot's formula (2.26). In order to obtain a simple result, we considered the case where the valence band is fully occupied and the conduction band is completely empty. While this description is valid for weak excitations, it breaks down for a strong optical excitation that generates many electron-hole pairs.

If we consider a finite occupation of electrons and holes, the semiconductor Bloch equation for the microscopic polarization becomes

$$\dot{p}_{\mathbf{k}}(t) = i(\omega_{\mathbf{k}} + i\gamma_{\mathbf{k}})p_{\mathbf{k}}(t) - \frac{i}{\hbar}(1 - f_{\mathbf{k}}^e - f_{\mathbf{k}}^h) \left(\sum_{\mathbf{q}} W_{\mathbf{q}} p_{\mathbf{k}+\mathbf{q}}(t) + \Omega_{\mathbf{k}}(t) \right). \quad (3.1)$$

Here we model the evolution of $p_{\mathbf{k}}$ and $f_{\mathbf{k}}^{e(h)}$ during and after a strong optical excitation. The inclusion of finite carrier populations appears in the equation above as a phase-space filling factor $(1 - f_{\mathbf{k}}^e - f_{\mathbf{k}}^h)$, screened Coulomb interaction $W_{\mathbf{q}} = \epsilon_{\mathbf{q}}^{-1}V_{\mathbf{q}}$, and renormalized electron-hole energy $\hbar\omega_{\mathbf{k}} = \epsilon_{\mathbf{k}}^c - \epsilon_{\mathbf{k}}^v - \Sigma_{\mathbf{k}}$. In the following, we describe the physical implications of each of these terms.

- The **phase-space filling** factor inhibits the Coulomb term and the light absorption. Moreover, in the case of population inversion, when there are more electrons in the conduction band than in the valence band ($f_{\mathbf{k}}^e > 1 - f_{\mathbf{k}}^h$), it can even reverse the sign of these terms, making the electron-hole interaction effectively repulsive and stimulating the emission of light.
- The additional¹ **dielectric screening** is caused by the excited charge-carriers (electrons and holes), and results in a weakening of the Coulomb interaction. The corresponding dielectric function is obtained using the Lindhard formula in the static limit [32, 33]. While this approach is sufficient to qualitatively describe the main effects of a large carrier density, a better quantitative description can be obtained using more sophisticated approaches that consider dynamic and excitonic screening.
- The **energy renormalization**, $\Sigma_{\mathbf{k}} = \Sigma^{\text{CH}} + \Sigma_{\mathbf{k}}^{\text{SX}}$, has two contributions called Coulomb-hole (CH) and screened-exchange (SX) self-energies. The first term, $\Sigma^{\text{CH}} = \sum_{\mathbf{q}} (V_{\mathbf{q}} - W_{\mathbf{q}})$, describes a reduction of the band-gap due to the screened electron-electron repulsion in the presence of many-particle dielectric screening. This is sometimes imagined as a *Coulomb-hole* that surrounds the electron. The second term, $\Sigma_{\mathbf{k}}^{\text{SX}} = \sum_{\mathbf{q}} W_{\mathbf{q}} (f_{\mathbf{k}+\mathbf{q}}^e + f_{\mathbf{k}+\mathbf{q}}^h)$, describes a reduction of the electron and

¹Note that, while the Coulomb interaction is already screened by the dielectric properties of the system in equilibrium, we are discussing here the additional screening coming from the excited charges.

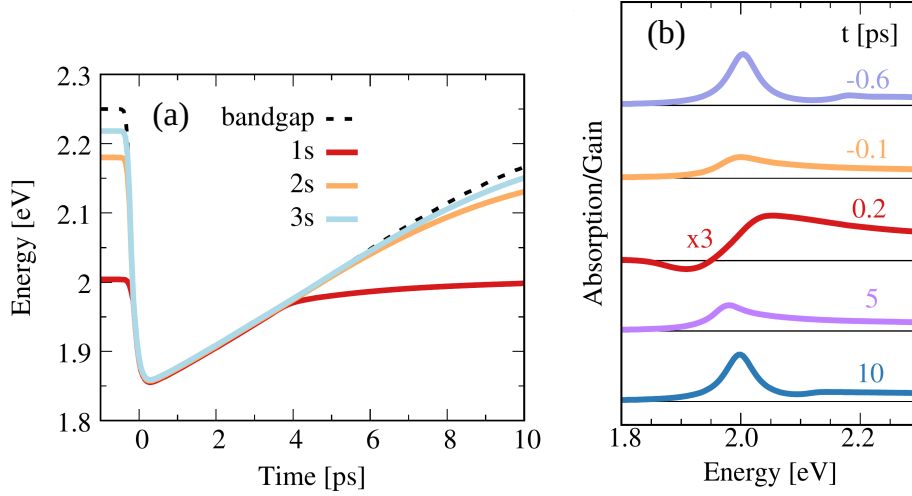


Figure 3.1: Influence of carrier density in the optical spectra of TMDs after an ultra-short optical excitation centered at $t = 0$. (a) Time-dependent energy renormalization for the single-particle bandgap and excitonic resonances. (b) Absorption spectra at different times after the optical excitation. Adapted from Ref. [34] (Paper II).

hole energies due to exchange interaction. Since the fermionic exchange interaction results in particles avoiding each other (Pauli-blocking), the decrease in energy is commonly described as a consequence of the *exchange hole* that surrounds each electron.

Another term that has appeared is the polarization decay (dephasing) $\gamma_{\mathbf{k}}$ due to electron-phonon scattering. Besides $\dot{p}_{\mathbf{k}}$, we also set up an equation of motion for the carrier occupations $f_{\mathbf{k}}^e, f_{\mathbf{k}}^h$ which include optical generation of carriers via polarization-to-population transfer and carrier thermalization by scattering with phonons. Since the most important features that we want to describe are contained in $\dot{p}_{\mathbf{k}}$, we do not include the equations for the carrier occupations here and refer the reader to Paper II or Refs. [16, 17, 29].

The calculated carrier occupations modify the exciton properties via screening and inhibiting or reversing the sign of the Coulomb interaction in the generalized Wannier equation shown in Paper II. In particular, the exciton binding energies are reduced for increasing densities, until there are no bound electron-hole pairs anymore. This transition from bound excitons to an un-

bound electron-hole plasma is called *Mott transition*. Such transition can be observed in Fig. 3.1(a) where, shortly after a very intense optical excitation, the exciton binding energies quickly vanish and the exciton resonances join the single-particle band-gap. The equilibrium is slowly recovered following the population decay.

We note here that this approach neglects the presence of two-particle and higher correlations. However, at the large carrier densities that we assume, where the system is dominated by an electron-hole plasma, our single-particle model—where all the other charges are treated as a mean field—should be sufficient to qualitatively describe the main phenomena.

The wavefunctions and exciton energies extracted from the generalized Wannier equation enter the Elliot formula for the optical absorption. The intensity of the absorption peak is bleached by phase-space filling and the decrease of the oscillator strength, whereas the absorption resonance position is modified due to the binding energy reduction and band-gap renormalization. Furthermore, in the extreme case of population inversion, the optical absorption reverses its sign, manifesting the effect of optical gain. Optical gain describes the situation in which the incident light, rather than being absorbed, stimulates the emission of more light. This effect is the basis for laser operation, and was experimentally observed in Ref. [35]. Our model captures both bleaching and optical gain, see Fig. 3.1(b). We also capture an initial red-shift followed by a blue-shift during the optical excitation that has been experimentally observed [36]. While the red-shift directly follows from the renormalization of the resonance energy, the subsequent blue-shift is caused by the bleaching of the lowest states such that optical absorption is only possible at higher energies where there are available states.

In Paper II, we use the microscopic theory described here for modeling pump-probe spectroscopy experiments. In this type of experiments, small variations in the optical absorption caused by the pump pulse are measured with a probe pulse, allowing to track the dynamics of the system. Our model provides a framework to understand the features of high carrier densities and population inversion in these experiments.

CHAPTER 4

Exciton dynamics

Immediately after an optical excitation, the photogenerated carriers start to thermalize into an equilibrium distribution. A comprehensive knowledge of the relaxation dynamics that occurs after the excitation provides important insights into other aspects such as transport and light emission. In this chapter, we discuss the ultra-fast relaxation of excitons into energetically-favourable states that are optically inactive. The relaxation of excitons into these so-called dark states was observed in Paper IV in a joint theory–experiment collaboration.

4.1 Dark-exciton formation

In Section 2.1.2, we introduced the band structure of TMDs (Fig. 2.1). This band structure has conduction-band minima at the $K^{(\prime)}$ and $\Lambda^{(\prime)}$ points of the Brillouin zone and valence-band maxima at $K^{(\prime)}$ and Γ . Excitonic states exist in all possible combinations of electron and hole valleys, e.g. KK , $K\Lambda$, KK' ,

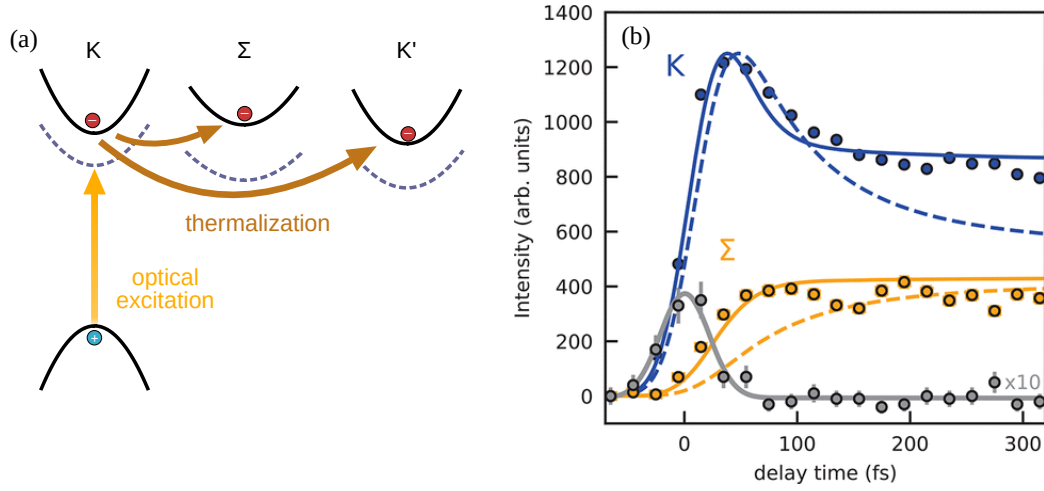


Figure 4.1: Dark-exciton formation resolved by trARPES. (a) Illustration of the process. An optical excitation generates an electron-hole pair that thermalizes throughout the Brillouin zone. Whereas the solid lines represent single-particle bands, the dashed lines illustrate the exciton binding. (b) ARPES signal (circles) and theoretical simulations of the electron occupation (dashed and solid lines) around each symmetry point. Gray dots and line are measurements and a Gaussian fit of the ARPES signal at the Γ point, which is a replica of the valence band that appears during the pulse excitation. Here Σ denotes the Λ valley. Figure adapted from Ref. [37] (Paper IV).

ΓK , etc. However, due to the small momentum carried by photons, only KK excitons with zero center-of-mass momentum can be optically active. For this reason, these are called bright states, while states with a momentum too large to be accessed by light are called momentum-dark states. Apart from momentum-dark states, there are also spin-dark states, where electron and hole have opposite spins, but throughout this work we disregard their effect in the dynamics since their formation time is slow compared to states where electron and hole have the same spin.

Because of their different binding energies, excitonic states might lie in a different ordering than the corresponding free electron-hole states. In particular, in tungsten-based TMDs, excitonic states at the KA and KK' valleys are the ones with lowest energy (see Fig. 2.2). This means that, while their electronic band structure would predict a direct band gap, these materials actually have an indirect band gap. This fact has major implications for the dynamics in

these materials [10]. Optically generated excitons at KK will relax into the energetically lower momentum-dark states (see Fig. 4.1(a)), which will then dominate the dynamics. Since such states cannot directly emit light, the radiative recombination time in these materials is rather slow [38, 39]. This fact is very relevant for optoelectronic devices such as photodetectors and solar cells, where the recombination is desired to be slow in order not to lose the charge-carriers that generate the electric current. An accurate understanding of the formation of momentum-dark excitons and their role in the dynamics is therefore crucial for the successful development of TMD-based devices.

The experimental detection of dark exciton states has been until recently only indirect, via optical features such as absorption linewidth [40] and phonon-assisted photoluminescence [41]. A tool that allows to directly map the whole energy landscape is angle-resolved photoemission spectroscopy (ARPES), where the electron energy and momentum is accurately determined. In Paper IV, our collaborators in the group of Ulrich Hofer (Marburg, Germany) directly observed the formation of momentum-dark excitons in WS₂ using time-resolved ARPES (trARPES). In the trARPES experiment, a coherent exciton population at KK and K'K' is generated by a linearly-polarized laser pulse. Coherent excitons with zero center-of-mass momentum quickly scatter with phonons and are transferred into incoherent population with finite momenta at the energetically lower KK', KΛ states¹ (see Fig. 4.1(a)) and their opposite-spin counterparts. The experiment, however, probes electrons and not whole excitons. Following the expansion scheme introduced in Ref. [30], the electron occupation at the valley v and momentum \mathbf{k} can be expressed in terms of the exciton occupation, $f_{\mathbf{k}}^v = \sum_{\nu_e \mathbf{Q}} |\phi_{\mathbf{k}-\alpha_e \mathbf{Q}}^{\nu_e}|^2 (|p^{\nu_e}|^2 \delta_{\mathbf{Q}\mathbf{0}} + N_{\mathbf{Q}}^{\nu_e})$. Thus, the electron occupation probed by the trARPES experiment reflects both coherent and incoherent exciton populations modeled by our microscopic theory. The measured and predicted electron occupations at K and Λ (Σ) are shown in Fig. 4.1(b), where the ultra-fast relaxation in a timescale of tens of femtoseconds is clearly observed. While the optical excitation and exciton thermalization are modeled following Eq. (2.30), the obtained microscopic insights on the ultra-fast formation of dark-excitons and the influence of coherent excitons are described in Paper IV.

¹Note that in Paper IV, Σ is used for the symmetry point that we call Λ. In literature, this symmetry point is called Σ, Λ, or Q.

CHAPTER 5

Exciton propagation

A crucial process in photodetectors is the transport of photoexcited charge-carriers to the leads. The underlying mechanisms that dominate the propagation must be thoroughly understood in order to determine the optimal conditions and limitations of these devices. In this chapter, we focus on the process of exciton diffusion and, in particular, reveal the origin of the fast propagation and formation of ring-shaped (halo) exciton distributions at high densities.

5.1 Conventional diffusion

In order to describe exciton diffusion, we start with the excitonic Hamiltonian described in Section 2.2.3. Now, however, the relevant quantity is not the (diagonal) occupation $N_{\mathbf{Q}} = \langle X_{\mathbf{Q}}^{\dagger} X_{\mathbf{Q}} \rangle$, but the off-diagonal elements $N_{\mathbf{Q}\mathbf{Q}'} = \langle X_{\mathbf{Q}}^{\dagger} X_{\mathbf{Q}'} \rangle$ that contain information about the spatial distribution. A more intuitive interpretation can be obtained by introducing the exciton Wigner

function $N_{\mathbf{Q}}(\mathbf{r}) = \sum_{\mathbf{q}} e^{i\mathbf{q}\cdot\mathbf{r}} \langle X_{\mathbf{Q}-\mathbf{q}/2}^\dagger X_{\mathbf{Q}+\mathbf{q}/2} \rangle$, which is the quasiprobability distribution for an exciton in the phase-space of momentum \mathbf{Q} and position \mathbf{r} . While the equations of motion for $N_{\mathbf{Q}\mathbf{Q}'}$ can be obtained directly from Heisenberg's equation of motion, the respective equations for $N_{\mathbf{Q}}(\mathbf{r})$ require more efforts. One way is to use Moyal brackets [42]. The approach we use was first introduced by Hess and Kuhn [43] and consists on first finding the equation of motion for $N_{\mathbf{Q}\mathbf{Q}'}$ and then Fourier-transforming to obtain the Wigner function. By Taylor-expanding the appearing terms, one can find the lowest-order contribution,

$$\dot{N}_{\mathbf{Q}}(\mathbf{r}, t) = -\mathbf{v}_{\mathbf{Q}} \cdot \nabla_{\mathbf{r}} N_{\mathbf{Q}}(\mathbf{r}, t) + \dot{N}_{\mathbf{Q}}(\mathbf{r}, t) \Big|_{\text{sc}}. \quad (5.1)$$

The first term describes propagation of excitons with velocity $\mathbf{v}_{\mathbf{Q}} = \hbar\mathbf{Q}M_X^{-1}$, where M_X is the total exciton mass. The neglected higher-order terms become important when the length-scale of spatial variations is very small, and would account for quantum-mechanical phenomena such as tunneling. The second term contains contributions accounting for exciton-phonon scattering, which we assume to be local (i.e. do not depend on other spatial coordinates) and are thus the same as in Eq. (2.30) but that now depend on the spatial position. Spatial profiles of the exciton density obtained by numerically solving this equation are shown in Fig. 5.1(a). The broadening of the spatial profile due to diffusion is illustrated by the red arrow. Note that the distribution is normalized at each time frame to illustrate the broadening. In this work, we consider only the valley that contains most of the exciton population and thus dominates the diffusion (see Paper VIII).

While we solve the equation of motion at this level, it is useful to rewrite the scattering term with a relaxation-time approach,

$$\dot{N}_{\mathbf{Q}}(\mathbf{r}, t) \Big|_{\text{sc}} = -\tau_{\mathbf{Q}}^{-1} (N_{\mathbf{Q}}(\mathbf{r}, t) - N_{\mathbf{Q}}^0(\mathbf{r}, t)),$$

where $\tau_{\mathbf{Q}}^{-1}$ is the relaxation time given by the scattering rates and $N_{\mathbf{Q}}^0(\mathbf{r}, t)$ is the exciton equilibrium (Boltzmann) distribution. At long time-scales, one can find that the time evolution of the exciton density, $N(\mathbf{r}) = \sum_{\mathbf{Q}} N_{\mathbf{Q}}(\mathbf{r}, t)$, corresponds to Fick's law,

$$\dot{N}(\mathbf{r}, t) = D\nabla^2 N(\mathbf{r}, t). \quad (5.2)$$

Furthermore, the exciton diffusion coefficient D can be related to the band-structure and exciton-phonon scattering rates. Assuming $\tau_{\mathbf{Q}} \approx \tau$, one recovers the well-known relation $D = \tau k_{\text{B}} T M_X^{-1}$. Thus, exciton propagation is in

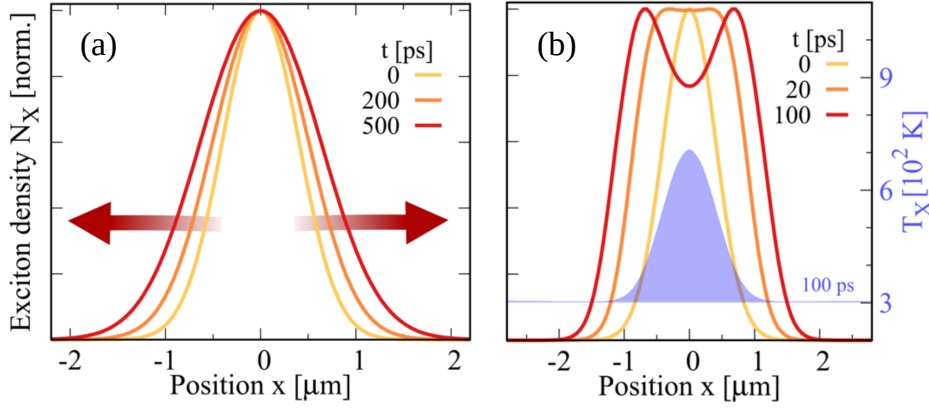


Figure 5.1: Time snaps of the spatial exciton distribution at (a) low and (b) high densities. The red arrows in (a) illustrate the diffusion process. The blue-shaded curve in (b) corresponds to exciton temperature (right axis). Figure adapted from Ref. [49] (Paper I).

general diffusive (as in Fig. 5.1(a)) and follows the conventional Fick's law. Several experiments have studied the propagation of excitons by performing time- and space-resolved photoluminescence (PL) measurements [44–48]. These works reported the diffusive propagation of excitons at low densities and more intriguing phenomena that appear at relatively high densities.

5.2 Non-linear propagation and halo formation

Conventional diffusion has been experimentally observed for low exciton densities. However, it was observed by Kulig et al. [44] that increasing the excitation density results in a faster diffusion and, eventually, the formation of ring-shaped PL spatial profiles—halos. This first study already pointed to exciton–exciton annihilation (EEA) as a possible origin for this phenomenon.

EEA is an Auger-like recombination process where two excitons scatter and one of them is annihilated whereas the other gains the corresponding energy. The exciton density thus decays following $\dot{N}(\mathbf{r}, t) = -r_A N^2(\mathbf{r}, t)$. Since the Auger coefficient r_A can be extracted from time-dependent pho-

toluminescence measurements [46], we can set up a semi-phenomenological model to describe the Auger recombination of an exciton with momentum \mathbf{Q} , $\dot{N}_{\mathbf{Q}}(\mathbf{r}, t)\Big|_{\text{A}} = -r_{\text{A}}N_{\mathbf{Q}}(\mathbf{r}, t)N(\mathbf{r}, t)$. This equation describes the annihilation of an exciton at \mathbf{Q} with an exciton in any state. We do not directly resolve the resulting high-energy exciton, but model its effect in the following way. The high-energy exciton resulting from Auger recombination will relax toward the ground state by emitting a cascade of phonons. Until now, we have treated phonons as a thermal bath. However, this sort of process where many excitons dissipate a large amount of energy by scattering with phonons will result in significantly increased non-equilibrium phonon populations that overheat the excitons. We take this into account by finding the equation of motion for the phonon number, including phonon emission cascade in a phenomenological manner, by assuming that the exciton energy is completely transferred to the phonons. Since we treat phonons in the Debye and Einstein models, we set a cut-off for the phonon momentum.

Auger recombination and the subsequent phonon emission cascade results in a heating of the exciton distribution. Importantly, the heating is more pronounced at the center of the excitation area, where the exciton density is largest, resulting in a temperature gradient. While the conventional diffusion equation (5.2) only considers a density gradient, a similar equation that considers the temperature gradient needs to be found. Considering that the exciton equilibrium distribution has a space-dependent temperature $T(\mathbf{r})$, the current density reads

$$\mathbf{j}(\mathbf{r}, t) = -D\nabla_{\mathbf{r}}N(\mathbf{r}, t) - s\nabla_{\mathbf{r}}T(\mathbf{r}, t), \quad (5.3)$$

where we have introduced the exciton Seebeck coefficient $s \approx \tau k_{\text{B}}NM_{\text{X}}^{-1}$. The second term corresponds to thermal drift and accounts for excitons moving from hotter to colder regions. Although we do not numerically solve this equation (we solve the equation for the exciton Wigner function), it is very useful for the purpose of understanding the origin of the non-linear propagation and halo formation. Initially, a strong thermal drift will result in a flat (super-Gaussian) density distribution, as excitons in the hot central region will propagate out faster than excitons in colder outer regions. This already results in non-linear propagation, i.e. the diffusion coefficient decreases with time. Moreover, if thermal drift is strong enough, the central region will continue to be emptied at a faster pace than excitons diffusing back. A significant temperature gradient can thus lead to the formation of a ring-like

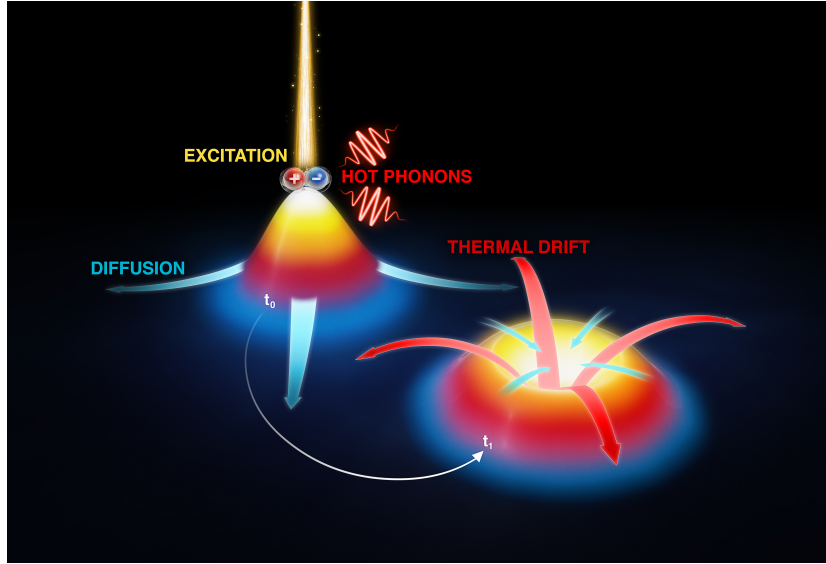


Figure 5.2: Schematic illustration of exciton propagation and halo formation. First, an optical excitation generates excitons that diffuse in order to homogenize the spatial distribution (t_0). Auger scattering and relaxation via phonon emission creates a long-lived spatial gradient in the exciton temperature (color gradient). The temperature gradient results in a strong thermal drift that drags excitons out of the central region, giving rise to the formation of a ring-shaped exciton distribution (t_1). Figure taken from Ref. [49] (Paper I).

shape in the spatial exciton distribution (see Fig. 5.1(b) and Fig. 5.2). Our microscopic model was able to prove that the Auger-recombination and the subsequent hot-phonon emission can heat the exciton population, leading to the observed non-trivial exciton propagation.

In later works, we have showed that the heating effects are not so strong in hBN-encapsulated TMDs due to the suppressed Auger scattering in this dielectric environment (Paper VI). Furthermore, in Paper XVI we have unveiled the mechanisms behind Auger recombination, and showed that the reduced Auger recombination in hBN compared to SiO_2 substrate is a result of the weaker Coulomb interaction and less optimal energetic landscape

CHAPTER 6

Exciton dissociation

Due to their charge neutrality, excitons cannot generate an electric current—only unbound electrons and holes can. However, electrons and holes in TMDs are bound into energetically-favourable excitons. This implies that, in order to generate an electric current, excitons must first *dissociate* into free electrons and holes. Since the dissociation process can be slow compared to transport, it poses a fundamental limit on the photoresponse in TMD-based photodetectors. In this Chapter, we discuss the process of exciton dissociation and, in particular, focus on dissociation via scattering with phonons.

6.1 Phonon-assisted dissociation

Previous studies have focused on dissociation of excitons assisted by an external (in-plane) electric field [50–52]. This mechanism consists in bound excitons tunneling into the continuum of unbound electron-hole states—a process that is facilitated by the bending of the potential landscape caused

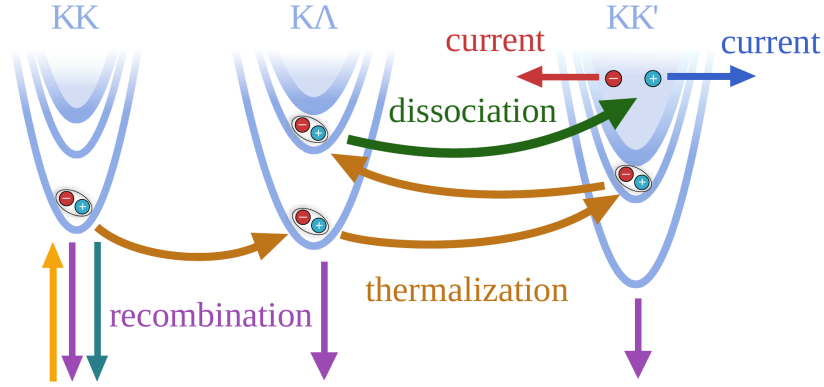


Figure 6.1: Schematic representation of exciton thermalization and dissociation in tungsten-based TMDs. Excitons are generated by an optical excitation in the KK valley. Then they scatter with phonons to reach a thermal equilibrium distribution, even dissociating into unbound electrons and holes. A weak external electric field drags the free carriers away, breaking the thermodynamic equilibrium and forcing a continuous dissociation. Excitons can recombine radiatively at KK or non-radiatively all around the Brillouin zone. Figure taken from Ref. [53] (Paper III).

by the applied field. However, extremely large electric fields are needed to dissociate tightly bound excitons with binding energies of hundreds of meV. For weaker electric fields, which might be more suitable for technological applications, dissociation will still occur but by other means. The dissociation mechanism that dominates at weak electric fields and low exciton densities is *phonon-assisted* dissociation. In Paper III, we tackle the problem of exciton dissociation via scattering with phonons and disentangle the main transition channels. Here we summarize the most important details of the theoretical model and the main results obtained.

While in previous chapters only the lowest exciton states (1s) have appeared, here we need to consider the whole Rydberg-like series of states, from the 1s state to the continuum of unbound states (see Fig. 2.2 and Fig. 6.1). As sketched in Fig. 6.1, excitons scatter with phonons to reach higher energetic states, and eventually dissociate into unbound electrons and holes by scattering into the continuum. The wavefunctions of both bound and continuum exciton states enter our model through the exciton-phonon matrix elements. All these states are obtained by numerically solving the Wannier equation. How-

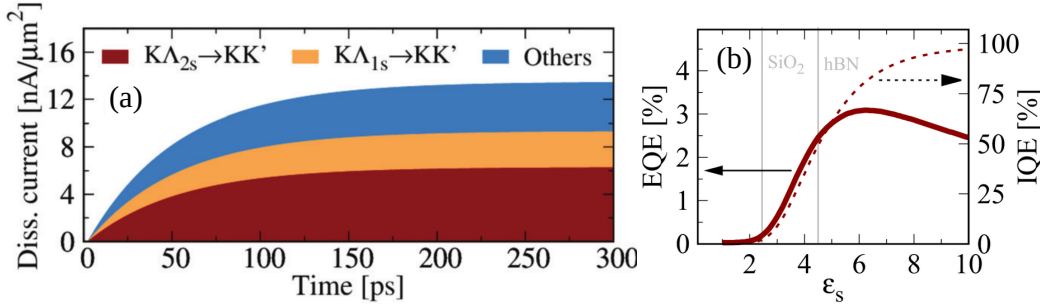


Figure 6.2: (a) Dissociation current as a function of time, disentangled into the main channels. (b) External (solid) and internal (dashed) quantum efficiencies as a function of the dielectric constant of the substrate or environment. Gray lines mark the dielectric constants corresponding to a SiO₂ substrate and hBN encapsulation. All simulations were performed for hBN-encapsulated WSe₂. Figure adapted from Ref. [53] (Paper III).

ever, the wavefunctions of continuum states are badly resolved in momentum space because they resemble a Dirac delta and their implementation in the exciton-phonon matrix elements is numerically demanding. To overtake this problem, we describe the continuum states with orthogonalized plane waves (OPWs). This corresponds to treating unbound electrons and holes as completely free particles (i.e. plane waves). Although this description does not capture characteristic features of Coulomb-correlated electron-hole pairs such as the Sommerfeld enhancement of optical absorption [54, 55], it is sufficient for the purpose of our work and reduces the numerical complexity. The combination of bound and free (plane-wave) states is correctly implemented by orthogonalizing the plane waves with respect to the bound-state wavefunctions. This step is necessary to obtain a complete set of wavefunctions and thus avoid unphysical overlaps. More information about the OPW approach can be found in the supplementary material of Paper III.

In Paper III, we consider a continuous optical excitation and study the microscopic mechanisms that govern exciton dissociation in the stationary state. We compute the dissociation current and disentangle it into the main contributions (see Fig. 6.2(a)). In this way, we are able to identify the main dissociation channels. In particular, for WSe₂ we find that most dissociation comes from excitons in the KA valley that scatter into the unbound continuum of KK'. This is a consequence of the strong coupling with phonons of

this inter-valley scattering channel. Furthermore, we are able to discern that it is mostly excitons in the 2s state that dissociate because of a trade-off between larger dissociation rates and lower occupation at higher energies closer to the continuum. The similarity between the dissociation-limited response time obtained of 50-100 ps and the one reported in Ref. [50] supports the validity of our model.

These findings are important to understand and predict the limitations and tunability of TMD-based photodetectors. For instance, the relative position of the Λ valley is strongly influenced by strain [56]. Thus, strain is a powerful knob that can be exploited to tune the photoresponse of TMDs. In Paper III, we study the influence of excitation energy, non-radiative recombination, dielectric screening, temperature, and strain on the photoresponse. Here, we show the impact of the dielectric constant of the environment, ϵ_s . We evaluate the external (EQE) and internal quantum efficiency (IQE), which are the ratio of excitons that dissociate with respect to incident and absorbed photon, respectively. For increasing screening, we find that both EQE and IQE increase (see Fig. 6.2(b)), reflecting more efficient dissociation due to less bound excitons that lie energetically closer to the continuum. For even stronger screening, however, we find that the EQE decreases, reflecting the weakening of the optical absorption because of the lower oscillator strength. The trade-off between dissociation and optical absorption results in the prediction that for photodetectors hBN encapsulation is a more optimal environment than a SiO_2 substrate.

In Paper III, we thoroughly describe the microscopic mechanisms behind exciton thermalization and dissociation. Besides disentangling the main dissociation channels and understanding why they dominate, we also resolve the exciton pathway by identifying the transitions with strongest scattering rate. Moreover, we provide a comprehensive study on the tunability of key quantities (EQE, IQE, response time) with external knobs and compare the performance of the four most relevant semiconducting TMDs.

CHAPTER 7

Charge transfer

The last fundamental process that we introduced in Fig. 1.3 is the collection of charge-carriers at the electrodes. The microscopic mechanisms that govern this process can determine the efficiency of the device, and their understanding is thus of crucial importance. In this Chapter, we describe the process of charge transfer in graphene–TMD van-der-Waals heterostructures and reveal the microscopic origin of the electron–hole asymmetry in the transfer rates.

7.1 Charge transfer in van der Waals heterostructures

One of the most obvious choices for electrodes in a TMD-based photodetector is graphene, due to its exceptional transport properties and the fact that it is a monolayer material as well. Few experimental works have studied charge-transfer in graphene-TMD heterostructures [57–61]. In these experiments,

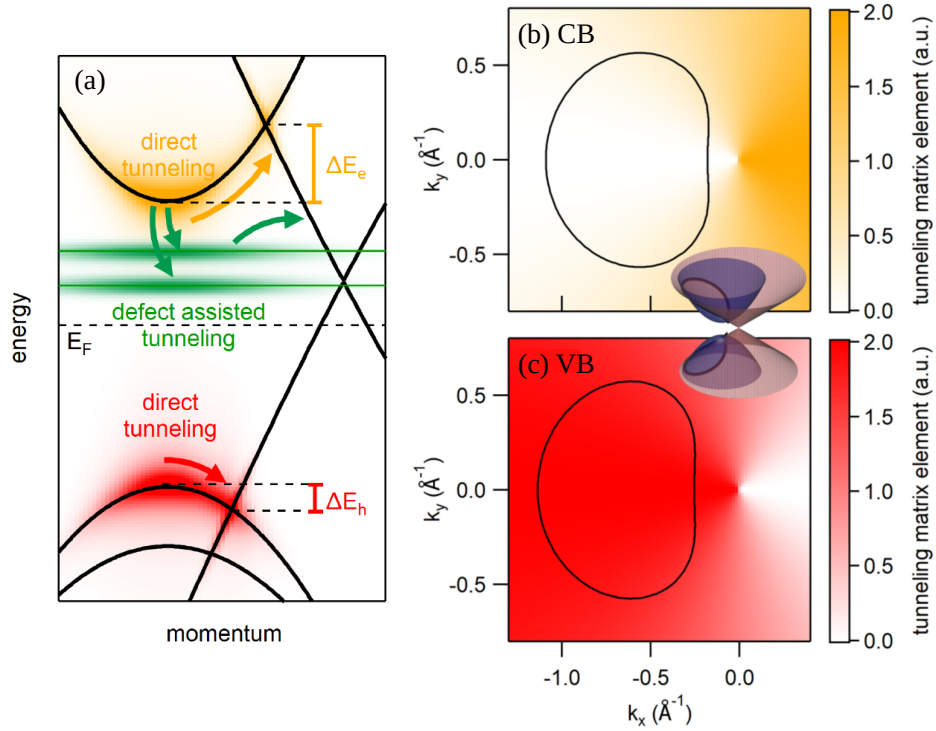


Figure 7.1: (a) Schematic representation of charge transfer in WS₂-graphene van-der-Waals heterostructures. (b)-(c) Tunneling matrix elements in momentum space for (b) conduction band (CB) and (c) valence band (VB). The origin is fixed to graphene’s K point. The solid line represents the intersection between WS₂ and graphene bands, which is illustrated by the inset. Figure adapted from Ref. [61] (Paper V).

an electron–hole pair is photoexcited in the TMD layer. The electron and hole in the TMD will tunnel into the graphene layer (see Fig. 7.1(a)) in order to relax to lower energies. What Ref. [59] in particular shows is that this transfer is faster for holes than for electrons, resulting in a charge separation that lasts for about 1 ps. In order to understand the origin of this asymmetric electron/hole transfer and the dominating transfer mechanism, we developed a microscopic model to describe the tunneling of electrons from one layer to the other. The results are presented in a joint theory–experiment study in Paper V. Here we summarize the main aspects of the microscopic model and the findings of our work.

In a graphene–TMD heterostructure, the parabolic and linear bands of the TMD and graphene, respectively, intersect and hybridize. In a simple approach that neglects hybridization and exciton populations (which is justified at the high densities considered here), the transfer dynamics can be described by a Boltzmann equation where the inter-layer tunneling occurs exactly at the band intersection¹. The transfer rates consist of the tunneling matrix elements—which provide the strength of the process—weighted by the carrier occupation at the intersection. Thus, the energy at the intersection with respect to the bottom (maximum) of the conduction (valence) band can be thought of as an energy barrier. In Fig. 7.1(a) it is clearly illustrated that the barrier for electrons in the conduction band is larger than for holes at the valence band. This simple reason could explain why holes tunnel faster than electrons, although the exact form of the tunneling matrix element still needs to be explored.

The tunneling matrix element contains information about the overlap between the electronic wavefunctions of both materials. A peculiar property of graphene is that the two atoms in the unit cell are of the same element—carbon. In consequence, the electron is in a superposition of two states that share the same properties but are not the same. This sub-lattice degree of freedom can be treated as a pseudo-spin. The electron is thus in a superposition of the two possible pseudo-spins. Graphene’s pseudospin is responsible for intriguing phenomena such as forbidden back-scattering and chiral tunneling [62]. The overlap between the wavefunctions of the TMD and graphene carry the momentum-dependent phase between the two graphene sub-lattices. This results in an interference effect that yields the angular dependence of the tunneling matrix element that is shown in Fig. 7.1(b)-(c). Since the relative phase in the conduction and valence bands differs by π , the shape of the tunneling matrix element is reversed in these two bands. The striking consequence is that, while tunneling at the conduction-band intersection is suppressed, it is maximized at the valence band. Therefore the faster tunneling of holes can be attributed to this phenomenon, in addition to the lower energy barrier. This theoretical prediction is very valuable for understanding the electron–hole tunneling asymmetry in TMD-graphene heterostructures.

¹In Fig. 7.1(a), defect-assisted tunneling is also illustrated. We do not consider this process in our microscopic model, but discuss its potential relevance in Paper V

CHAPTER 8

Conclusion and outlook

In this thesis, we have provided a microscopic understanding of the fundamental many-particle mechanisms that govern the main processes in TMD-based photodetectors. The theoretical approach presented here is based on the density matrix formalism and describes a system of interacting electrons, phonons, and photons. In particular, we have used our model to study the influence of excitons on the optical response, transport, and dynamics in TMD monolayers. Our work provides relevant insights on (1) the density-dependence of optical absorption spectra, (2) the dominant role of momentum-dark excitons in the relaxation and dissociation dynamics, (3) the formation of photoluminescence halos at large exciton densities, and (4) the asymmetric charge transfer in WS_2 -graphene heterostructures. The microscopic understanding of these processes contributes to determining the optimal operation conditions, limitations and tunability of TMD-based photodetectors.

While in this thesis we have focused on studying monolayers of TMDs—with the only exception of Chapter 7—a lot of the current research in the field

focuses on investigating van-der-Waals heterostructures, which are formed by two or more monolayer materials that are held together via van der Waals interaction. These structures are highly tunable with the relative twist angle between the two monolayers and offer a platform for studying intriguing many-body phenomena, including strongly correlated electrons and moiré-localized localized excitons. Moreover, many-particle states beyond excitons become relevant with doping, high excitation power, temperature and strong light-matter interaction. Examples of these are trions—three-particle complexes formed by two electrons (holes) and one hole (electron)—, biexcitons—formed by two excitons—, and different sorts of exciton-polarons (exciton-phonon, exciton-polariton, exciton Fermi-polarons, etc.). In particular, trions and Fermi-polarons become very relevant at finite doping, with a significant impact on the optical absorption and emission spectra, that can be partially or almost completely dominated by these energetically-favourable species [63]. Since in actual devices doping will play an important role, the impact of trions in both monolayers and van-der-Waals heterostructures must be accurately understood. An extension of the work presented in this thesis to include the influence of trions will provide a more complete picture of the main many-particle processes that govern the operation of TMD-based optoelectronic devices.

Acknowledgments

First of all, I would like to thank my supervisor, Ermin Malic, for his constant support, motivation, and guidance. I would also like to thank my colleague Samuel Brem for his important insights and stimulating discussions—his passion for physics is contagious.

I further thank my examiner, Jari Kinaret, for carefully reading my thesis, and Janine Splettstoesser for taking the time to be my opponent (I hope that you enjoy reading this thesis).

Moreover, I thank all the members of the Ultrafast Quantum Dynamics group in Marburg and Chalmers, and specially Daniel Erkensten and Joakim Hagel for the interesting conversations during coffee and lunch breaks.

Finally, the people that give me strength during the good and bad days are my family, friends and specially Gemma (gràcies per tot).

Bibliography

- [1] Kostya S Novoselov, Andre K Geim, Sergei V Morozov, De-eng Jiang, Yanshui Zhang, Sergey V Dubonos, Irina V Grigorieva, and Alexandr A Firsov. Electric field effect in atomically thin carbon films. *Science*, 306(5696):666–669, 2004.
- [2] Kostya S Novoselov, D Jiang, F Schedin, TJ Booth, VV Khotkevich, SV Morozov, and Andre K Geim. Two-dimensional atomic crystals. *Proceedings of the National Academy of Sciences*, 102(30):10451–10453, 2005.
- [3] Kostya S Novoselov, Andre K Geim, Sergei Vladimirovich Morozov, Dingde Jiang, Michail I Katsnelson, IV Grigorieva, SV Dubonos, and AA Firsov. Two-dimensional gas of massless dirac fermions in graphene. *Nature*, 438(7065):197–200, 2005.
- [4] Kin Fai Mak, Changgu Lee, James Hone, Jie Shan, and Tony F Heinz. Atomically thin MoS₂: a new direct-gap semiconductor. *Physical Review Letters*, 105(13):136805, 2010.
- [5] Andrea Splendiani, Liang Sun, Yuanbo Zhang, Tianshu Li, Jonghwan

- Kim, Chi-Yung Chim, Giulia Galli, and Feng Wang. Emerging photoluminescence in monolayer MoS₂. *Nano Letters*, 10(4):1271–1275, 2010.
- [6] Qing Hua Wang, Kouros Kalantar-Zadeh, Andras Kis, Jonathan N Coleman, and Michael S Strano. Electronics and optoelectronics of two-dimensional transition metal dichalcogenides. *Nature Nanotechnology*, 7(11):699–712, 2012.
- [7] Andre K Geim and Irina V Grigorieva. Van der waals heterostructures. *Nature*, 499(7459):419–425, 2013.
- [8] Xiaofeng Qian, Junwei Liu, Liang Fu, and Ju Li. Quantum spin hall effect in two-dimensional transition metal dichalcogenides. *Science*, 346(6215):1344–1347, 2014.
- [9] Oriol Lopez-Sanchez, Dominik Lembke, Metin Kayci, Aleksandra Radenovic, and Andras Kis. Ultrasensitive photodetectors based on monolayer MoS₂. *Nature Nanotechnology*, 8(7):497–501, 2013.
- [10] Thomas Mueller and Ermin Malic. Exciton physics and device application of two-dimensional transition metal dichalcogenide semiconductors. *npj 2D Materials and Applications*, 2(1):1–12, 2018.
- [11] Gang Wang, Alexey Chernikov, Mikhail M Glazov, Tony F Heinz, Xavier Marie, Thierry Amand, and Bernhard Urbaszek. Colloquium: Excitons in atomically thin transition metal dichalcogenides. *Reviews of Modern Physics*, 90(2):021001, 2018.
- [12] Branimir Radisavljevic, Aleksandra Radenovic, Jacopo Brivio, Valentina Giacometti, and Andras Kis. Single-layer MoS₂ transistors. *Nature Nanotechnology*, 6(3):147–150, 2011.
- [13] Sajedeh Manzeli, Dmitry Ovchinnikov, Diego Pasquier, Oleg V Yazyev, and Andras Kis. 2d transition metal dichalcogenides. *Nature Reviews Materials*, 2(8):1–15, 2017.
- [14] Alexey Chernikov, Timothy C Berkelbach, Heather M Hill, Albert Rigosi, Yilei Li, Ozgur Burak Aslan, David R Reichman, Mark S Hybertsen, and Tony F Heinz. Exciton binding energy and nonhydrogenic rydberg series in monolayer WS₂. *Physical Review Letters*, 113(7):076802, 2014.

- [15] Keliang He, Nardeep Kumar, Liang Zhao, Zefang Wang, Kin Fai Mak, Hui Zhao, and Jie Shan. Tightly bound excitons in monolayer WSe₂. *Physical Review Letters*, 113(2):026803, 2014.
- [16] Ermin Malic and Andreas Knorr. *Graphene and carbon nanotubes: ultrafast optics and relaxation dynamics*. John Wiley & Sons, 2013.
- [17] Hartmut Haug and Stephan W Koch. *Quantum theory of the optical and electronic properties of semiconductors*. World Scientific Publishing Company, 2009.
- [18] Wolfgang Nolting and William D Brewer. *Fundamentals of Many-body Physics*. Springer, 2008.
- [19] Mackillo Kira and Stephan W Koch. *Semiconductor quantum optics*. Cambridge University Press, 2011.
- [20] Gerald D Mahan. *Many-Particle Physics*. Springer US, 2000.
- [21] Andor Kormányos, Guido Burkard, Martin Gmitra, Jaroslav Fabian, Viktor Zólyomi, Neil D Drummond, and Vladimir Fal'ko. k · p theory for two-dimensional transition metal dichalcogenide semiconductors. *2D Materials*, 2(2):022001, 2015.
- [22] Zhenghe Jin, Xiaodong Li, Jeffrey T Mullen, and Ki Wook Kim. Intrinsic transport properties of electrons and holes in monolayer transition-metal dichalcogenides. *Physical Review B*, 90(4):045422, 2014.
- [23] Hongyi Yu, Gui-Bin Liu, Pu Gong, Xiaodong Xu, and Wang Yao. Dirac cones and dirac saddle points of bright excitons in monolayer transition metal dichalcogenides. *Nature Communications*, 5(1):1–7, 2014.
- [24] Diana Y Qiu, Ting Cao, and Steven G Louie. Nonanalyticity, valley quantum phases, and lightlike exciton dispersion in monolayer transition metal dichalcogenides: Theory and first-principles calculations. *Physical Review Letters*, 115(17):176801, 2015.
- [25] N S. Rytova. The screened potential of a point charge in a thin film. *Moscow University Physics Bulletin*, 3(3):18, 1967.

- [26] L. V. Keldysh. Coulomb interaction in thin semiconductor and semimetal films. *Soviet Journal of Experimental and Theoretical Physics Letters*, 29:658, June 1979.
- [27] Ting Cao, Gang Wang, Wenpeng Han, Huiqi Ye, Chuanrui Zhu, Junren Shi, Qian Niu, Pingheng Tan, Enge Wang, Baoli Liu, et al. Valley-selective circular dichroism of monolayer molybdenum disulphide. *Nature Communications*, 3(1):1–5, 2012.
- [28] M Lindberg and Stephan W Koch. Effective bloch equations for semiconductors. *Physical Review B*, 38(5):3342, 1988.
- [29] Mackillo Kira and Stephan W Koch. Many-body correlations and excitonic effects in semiconductor spectroscopy. *Progress in quantum electronics*, 30(5):155–296, 2006.
- [30] Florian Katsch, Malte Selig, Alexander Carmele, and Andreas Knorr. Theory of exciton–exciton interactions in monolayer transition metal dichalcogenides. *physica status solidi (b)*, 255(12):1800185, 2018.
- [31] AL Ivanov and H Haug. Self-consistent theory of the biexciton optical nonlinearity. *Physical Review B*, 48(3):1490, 1993.
- [32] Jens Lindhard. On the properties of a gas of charged particles. *Kgl. Danske Videnskab. Selskab Mat.-fys. Medd.*, 28:8, 1954.
- [33] Frank Stern. Polarizability of a two-dimensional electron gas. *Physical Review Letters*, 18(14):546, 1967.
- [34] Raül Perea-Causín, Samuel Brem, and Ermin Malic. Microscopic modeling of pump–probe spectroscopy and population inversion in transition metal dichalcogenides. *physica status solidi (b)*, 257(12):2000223, 2020.
- [35] Alexey Chernikov, Claudia Ruppert, Heather M Hill, Albert F Rigosi, and Tony F Heinz. Population inversion and giant bandgap renormalization in atomically thin WS₂ layers. *Nature Photonics*, 9(7):466–470, 2015.
- [36] Edbert J Sie, Alexander Steinhoff, Christopher Gies, Chun Hung Lui, Qiong Ma, Malte Rosner, Gunnar Schönhoff, Frank Jahnke, Tim O Wehling, Y-H Lee, et al. Observation of exciton redshift–blueshift crossover in monolayer WS₂. *Nano Letters*, 17(7):4210–4216, 2017.

- [37] Robert Wallauer, Raul Perea-Causin, Lasse Münster, Sarah Zajusch, Samuel Brem, Jens Gütde, Katsumi Tanimura, Kai-Qiang Lin, Rupert Huber, Ermin Malic, and Ulrich Höfer. Momentum-resolved observation of exciton formation dynamics in monolayer WS_2 . *Nano Letters*, 21(13):5867–5873, 2021.
- [38] Malte Selig, Gunnar Berghäuser, Marten Richter, Rudolf Bratschitsch, Andreas Knorr, and Ermin Malic. Dark and bright exciton formation, thermalization, and photoluminescence in monolayer transition metal dichalcogenides. *2D Materials*, 5(3):035017, 2018.
- [39] Xiao-Xiao Zhang, Yumeng You, Shu Yang Frank Zhao, and Tony F Heinz. Experimental evidence for dark excitons in monolayer WSe_2 . *Physical Review Letters*, 115(25):257403, 2015.
- [40] Malte Selig, Gunnar Berghäuser, Archana Raja, Philipp Nagler, Christian Schüller, Tony F Heinz, Tobias Korn, Alexey Chernikov, Ermin Malic, and Andreas Knorr. Excitonic linewidth and coherence lifetime in monolayer transition metal dichalcogenides. *Nature Communications*, 7(1):1–6, 2016.
- [41] Samuel Brem, August Ekman, Dominik Christiansen, Florian Katsch, Malte Selig, Cedric Robert, Xavier Marie, Bernhard Urbaszek, Andreas Knorr, and Ermin Malic. Phonon-assisted photoluminescence from indirect excitons in monolayers of transition-metal dichalcogenides. *Nano Letters*, 20(4):2849–2856, 2020.
- [42] José E Moyal. Quantum mechanics as a statistical theory. In *Mathematical Proceedings of the Cambridge Philosophical Society*, volume 45, pages 99–124. Cambridge University Press, 1949.
- [43] Ortwin Hess and Tilmann Kuhn. Maxwell-bloch equations for spatially inhomogeneous semiconductor lasers. i. theoretical formulation. *Physical Review A*, 54(4):3347, 1996.
- [44] Marvin Kulig, Jonas Zipfel, Philipp Nagler, Sofia Blanter, Christian Schüller, Tobias Korn, Nicola Paradiso, Mikhail M Glazov, and Alexey Chernikov. Exciton diffusion and halo effects in monolayer semiconductors. *Physical Review Letters*, 120(20):207401, 2018.

- [45] F Cadiz, Cédric Robert, E Courtade, M Manca, L Martinelli, T Taniguchi, K Watanabe, Thierry Amand, ACH Rowe, D Paget, et al. Exciton diffusion in WSe₂ monolayers embedded in a van der waals heterostructure. *Applied Physics Letters*, 112(15):152106, 2018.
- [46] Shinichiro Mouri, Yuhei Miyauchi, Minglin Toh, Weijie Zhao, Goki Eda, and Kazunari Matsuda. Nonlinear photoluminescence in atomically thin layered WSe₂ arising from diffusion-assisted exciton-exciton annihilation. *Physical Review B*, 90(15):155449, 2014.
- [47] Long Yuan, Ti Wang, Tong Zhu, Mingwei Zhou, and Libai Huang. Exciton dynamics, transport, and annihilation in atomically thin two-dimensional semiconductors. *The Journal of Physical Chemistry Letters*, 8(14):3371–3379, 2017.
- [48] Jonas Zipfel, Marvin Kulig, Raúl Perea-Causín, Samuel Brem, Jonas D Ziegler, Roberto Rosati, Takashi Taniguchi, Kenji Watanabe, Mikhail M Glazov, Ermin Malic, et al. Exciton diffusion in monolayer semiconductors with suppressed disorder. *Physical Review B*, 101(11):115430, 2020.
- [49] Raul Perea-Causin, Samuel Brem, Roberto Rosati, Roland Jago, Marvin Kulig, Jonas D Ziegler, Jonas Zipfel, Alexey Chernikov, and Ermin Malic. Exciton propagation and halo formation in two-dimensional materials. *Nano Letters*, 19(10):7317–7323, 2019.
- [50] Mathieu Massicotte, Fabien Vialla, Peter Schmidt, Mark B Lundberg, Simone Latini, Sten Hastrup, Mark Danovich, Diana Davydovskaya, Kenji Watanabe, Takashi Taniguchi, et al. Dissociation of two-dimensional excitons in monolayer WSe₂. *Nature Communications*, 9(1):1–7, 2018.
- [51] Sten Hastrup, Simone Latini, Kirill Bolotin, and Kristian S Thygesen. Stark shift and electric-field-induced dissociation of excitons in monolayer MoS₂ and h-BN/MoS₂ heterostructures. *Physical Review B*, 94(4):041401, 2016.
- [52] Høgni C Kamban and Thomas G Pedersen. Field-induced dissociation of two-dimensional excitons in transition metal dichalcogenides. *Physical Review B*, 100(4):045307, 2019.

- [53] Raúl Perea-Causín, Samuel Brem, and Ermin Malic. Phonon-assisted exciton dissociation in transition metal dichalcogenides. *Nanoscale*, 13(3):1884–1892, 2021.
- [54] RJ Elliott. Intensity of optical absorption by excitons. *Physical Review*, 108(6):1384, 1957.
- [55] Masaki Shinada and Satoru Sugano. Interband optical transitions in extremely anisotropic semiconductors. i. bound and unbound exciton absorption. *Journal of the Physical Society of Japan*, 21(10):1936–1946, 1966.
- [56] Zahra Khatibi, Maja Feierabend, Malte Selig, Samuel Brem, Christopher Linderälv, Paul Erhart, and Ermin Malic. Impact of strain on the excitonic linewidth in transition metal dichalcogenides. *2D Materials*, 6(1):015015, 2018.
- [57] Jiaqi He, Nardeep Kumar, Matthew Z Bellus, Hsin-Ying Chiu, Dawei He, Yongsheng Wang, and Hui Zhao. Electron transfer and coupling in graphene–tungsten disulfide van der waals heterostructures. *Nature Communications*, 5(1):1–5, 2014.
- [58] Mathieu Massicotte, Peter Schmidt, Fabien Violla, Kevin G Schädler, Antoine Reserbat-Plantey, Kenji Watanabe, Takashi Taniguchi, Klaas-Jan Tielrooij, and Frank HL Koppens. Picosecond photoresponse in van der waals heterostructures. *Nature Nanotechnology*, 11(1):42–46, 2016.
- [59] Sven Aeschlimann, Antonio Rossi, Mariana Chávez-Cervantes, Razvan Krause, Benito Arnoldi, Benjamin Stadtmüller, Martin Aeschlimann, Stiven Forti, Filippo Fabbri, Camilla Coletti, et al. Direct evidence for efficient ultrafast charge separation in epitaxial WS₂/graphene heterostructures. *Science Advances*, 6(20):eaay0761, 2020.
- [60] Long Yuan, Ting-Fung Chung, Agnieszka Kuc, Yan Wan, Yang Xu, Yong P Chen, Thomas Heine, and Libai Huang. Photocarrier generation from interlayer charge-transfer transitions in WS₂-graphene heterostructures. *Science Advances*, 4(2):e1700324, 2018.
- [61] R Krause, S Aeschlimann, M Chavez-Cervantes, R Perea-Causin, S Brem, E Malic, S Forti, F Fabbri, C Coletti, and I Gierz. Microscopic

understanding of ultrafast charge transfer in van-der-waals heterostructures. *arXiv preprint arXiv:2012.09268*, 2020.

- [62] MI Katsnelson, KS Novoselov, and AK Geim. Chiral tunnelling and the klein paradox in graphene. *Nature Physics*, 2(9):620–625, 2006.
- [63] Meinrad Sidler, Patrick Back, Ovidiu Cotlet, Ajit Srivastava, Thomas Fink, Martin Kroner, Eugene Demler, and Atac Imamoglu. Fermi polaron-polaritons in charge-tunable atomically thin semiconductors. *Nature Physics*, 13(3):255–261, 2017.